Arsenic speciation in multiple metal environments
II. Micro-spectroscopic investigation of a CCA contaminated soil

Markus Gräfe [a,*,1], Ryan V. Tappero [a], Matthew A. Marcus [b], Donald L. Sparks [a]

[a] *Environmental Soil Chemistry Group, Department of Plant and Soil Sciences, 152 Townsend Hall, University of Delaware, Newark, DE 19717-1303, USA*
[b] *Advanced Light Source, 10.3.2, Lawrence Berkeley National Laboratories, Berkeley, CA 94720, USA*

Abstract

The speciation of arsenic (As) in a copper-chromated-arsenate (CCA) contaminated soil was investigated using micro-focused X-ray fluorescence (μXRF) and micro-focused X-ray absorption fine structure (μXAFS) spectroscopies to determine if and how the co-contaminating metal cations (Cu, Zn, Cr) influenced the speciation of As. 15 μXRF images were collected on 30-μm polished thin sections and powder-on-tape samples from which Pearson correlation coefficients (ρ) between As and various metal species were determined based on the fluorescence intensity of each element in each image pixel. 29 μXAFS and two bulk-XAFS spectra were collected from depths of 0–20 cm (LM-A) and 20–40 cm (LM-B) to determine the chemical speciation of As in the soil by target analyses of principal components with *circa* 52 reference spectra and linear least-square combination fitting of individual experimental spectra with a refined reference phase list (32) of likely As species. Arsenic and metal cations (Cr, Mn, Fe, Cu, Zn) accumulated in distinct, isolated areas often not larger than 50×50 μm in which the Pearson correlation between the elements was strongly positive ($\rho > 0.75$). The correlation of As to Zn and Cr decreased from >0.9 to <0.8 and increased to Cu from ~0.6 to >0.8 with depth. Arsenic occurred predominantly in the +5 oxidation state. Abstract factor analysis and linear least square combination fit analysis suggested that As occurred as a continuum of fully and poorly-ordered copper-arsenate precipitates with additional components being characterized by surface adsorption complexes on goethite and gibbsite in the presence and absence of Zn. Precipitates other than copper-based ones, e.g., scorodite, adamite and ojuelaite were also identified. The significant co-localization and chemical speciation of As with Cu suggest that the speciation of As in a contaminated soils is not solely controlled by surface adsorption reactions, but significantly influenced by the co-contaminating metal cation fraction. Future studies into As contaminated soil therefore need to focus on identifying the speciation of As and the co-localizing metal cations.

1. Introduction

Arsenic (As) is a highly toxic element that has been released into the environment by anthropogenic processes and weathering of As bearing minerals [1,2]. Arsenic contamination occurs commonly in areas where metal contamination is the prevalent problem due to the refinement of common parent materials or the application of mixed metal–arsenic substances (acid mine drainage, smelter wastes, pesticides, chromated copper arsenate, aka CCA) [3–5]. The remediation strategy of such sites is often targeted at stabilizing the more abundant metal fraction, for example, by liming with dolomite ([Ca, Mg]CO$_3$), and thereby raising the soil solution pH [6]. The pH-dependent sorption/desorption behavior of arsenate and other oxyanions (CrO$_4$, PO$_4$, SeO$_4$) is dissimilar to that of metals with liming potentially causing desorption and mobilization of As from variably charged soil surfaces. In well-aerated environments, As exists primarily as an oxo-acid, arsenate (as $As^{5+} = H_nAsO_4^{(n-3)} = As(V) = $ arsenate), which adsorbs on iron- and aluminium-oxide surfaces via ligand-exchange reactions resulting in the formation of predominantly bidentate binuclear surface species [7–11].

---

* Corresponding author. Fax: +1 61 2 9351 5108.
  E-mail address: m.grafe@usyd.edu.au (M. Gräfe).
[1] Current address: Faculty of Agriculture, Food & Natural Resources, Ross Street Building (A03), Room 322, The University of Sydney, NSW 2006, Australia.

Recently we have shown that Zn and arsenate form co-precipitates of differing structures at pH 7 depending on the density of goethite in solution [12,13]. Under mildly acidic conditions, these precipitates re-dissolved after a 6-month aging period, suggesting that these phases were metastable [13]. Phosphatic minerals, including the subclass of arsenate minerals, contain PO_4 and AsO_4, which act as insular units in Cu-, Zn-, and Pb-hydroxides [14]. Metal co-precipitation products containing As have to date been sparingly shown to exist, but ferric-arsenate (scorodite) and arsenate-substituted jarosites have been identified in naturally- and industrially-contaminated environments, respectively [15,16]. Based on thermodynamic calculations, Sadiq [17] suggested that in acidified soil environments, Fe- and Al-arsenates controlled As solubility, while at high pH, $Ca_3(AsO_4)_2$ controlled As solubility, highlighting that pH mainly governs which ions become active in the sequestration of arsenic. In the companion paper of this manuscript [18], As(V) was coordinated by Cu(II) rather than Al ions on gibbsite at pH 7. On silica (pH 7), As(V) and Zn formed a koettigite-like precipitate, whereas As(V) sorption complexes on goethite (pH 7) in the presence of Cu(II) and/or Zn(II) could not be distinguished from the As(V) surface complexes formed in their absence. The incorporation of AsO_4 ligands into the structure of metal-hydroxide precipitates or the coordination of AsO_4 on mineral surfaces by co-contaminating metal cations are important reaction mechanisms by which As(V) can be immobilized in the environment. While laboratory studies have shown first row transition metals to form precipitates with As(V) on goethite, it is unclear if such precipitates also form in contaminated environments with multiple metals, multiple mineral surfaces, and multiple competing ligands (e.g., humic and fulvic acids). The objective of our study was to determine if and how the solid-phase speciation of As in a copper chromated arsenate (CCA-) and Zn-contaminated soil was influenced by the co-contaminating metal cations.

2. Materials and methods

2.1. Soil characterization

Soil samples from depths of 0–20 cm (LM-A) and 20–40 cm (LM-B) were collected from a former timber/lumber treatment site (shut down in 1953) near the University of Florida (Gainesville, FL), and sealed into 5-L plastic buckets. The fractions were analyzed for total metal ion content (HNO_3 digestion), soil pH (1:5 $CaCl_2$), particle size distribution, organic
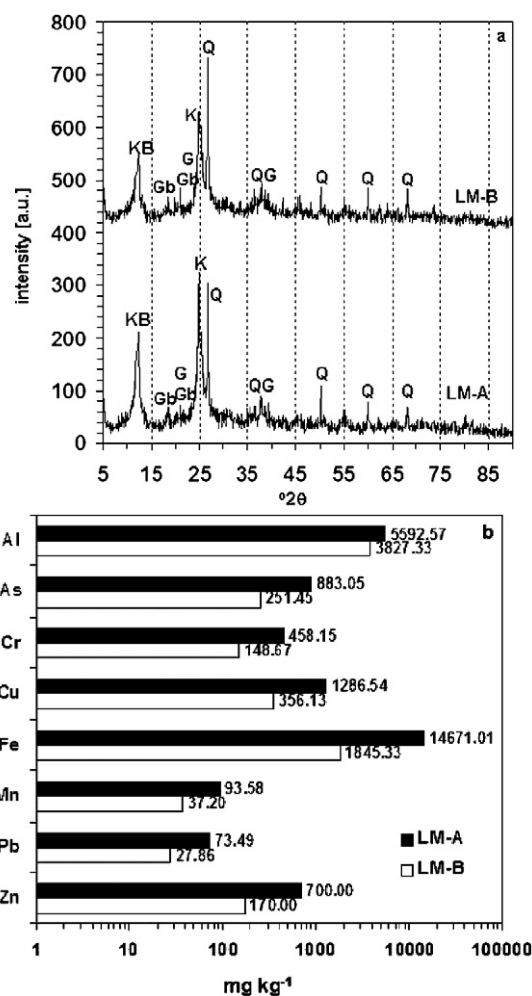

Fig. 1. (a) XRD patterns of LM-A and LM-B soil fractions. B = birnessite, G = goethite, Gb = gibbsite, K = kaolinite, Q = quartz. (b) Bulk elemental concentrations were determined from a total HNO_3 acid digest.

matter content (loss on ignition, LOI), and cation exchange capacity (CEC) (pH 7 and 5.5) [19]. The major primary and secondary clay minerals were identified by bulk X-ray diffraction using standard procedures (ibid.). The results of the soil characterization are summarized in Fig. 1 and Table 1.

2.2. Replenishment desorption study

A replenishment desorption study was carried out by suspending ca. 0.30 g of either LM-A or LM-B soil in 30 ml

Table 1
Soil characterization

Soil	pH	% sand[a]	% silt	% clay	OM (wt%)[b]	CEC (pH 7)[c]	CEC (pH 5)[d]	Crystalline components[e]
LM-A	7.0–7.5	82	15	3	2.9	10.06	6.67	G, Gb, K, Q
LM-B	7.0–7.5	85	14	1	1.2	6.06	3.78	G, Gb, K, Q

[a] % sand, silt, and clay fraction determined from hydrometer readings after settling times in 80 mM hexa-metaphosphate of 30 s and 2 h.
[b] Determined by loss on ignition.
[c] Mg/Ca exchange at pH 7; units = meq_c 100 g^{-1} soil.
[d] Acetate exchange at pH 5; units = meq_c 100 g^{-1} soil.
[e] Bulk X-ray diffraction, $\lambda = 1.5406$ Å. G = goethite, Gb = gibbsite, K = kaolinite, Q = quartz.
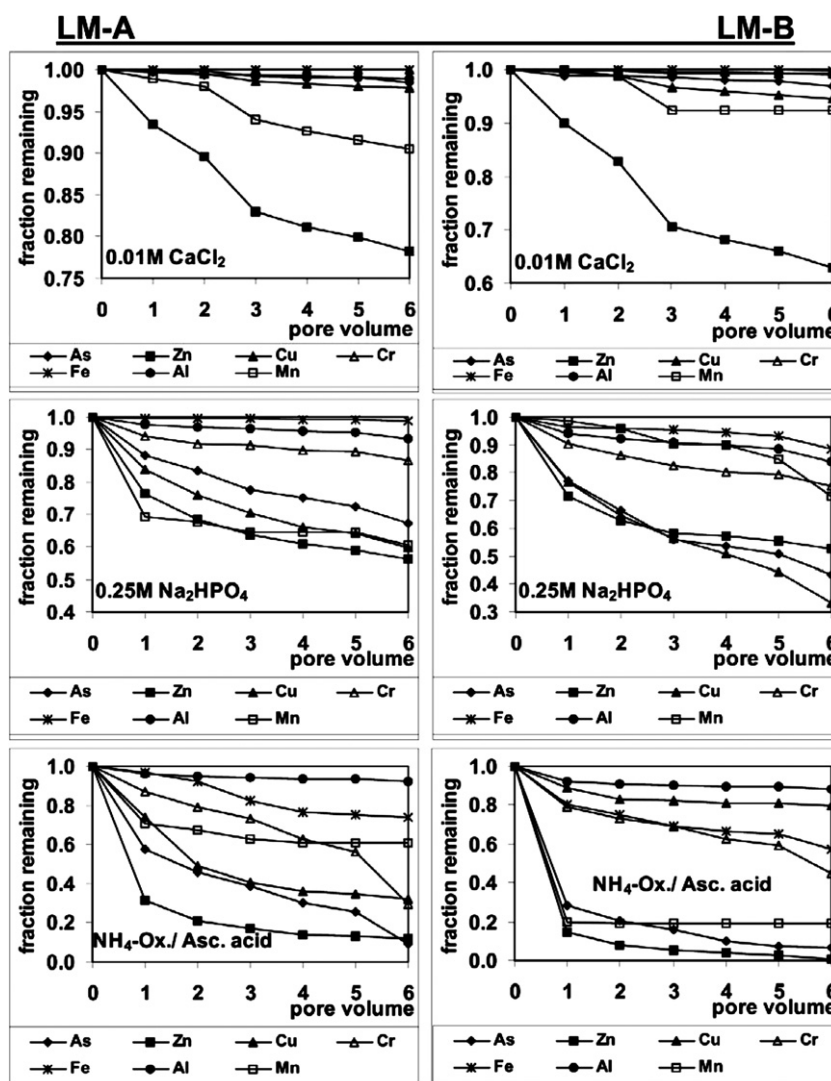
Fig. 2. Replenishment desorption study for LM-A and LM-B. Arsenic, Cr, Cu, and Zn were more labile in LM-B than in LM-A. Zinc appeared to be more labile than the other metals, which suggests that it may have had a different (shorter) residence time or a different application history.

desorbing solution and shaking the suspensions for 20- and 30-min, 1-h, twice 2-h, and one 24-h period. After each shaking period, the suspensions were centrifuged at 12,000 rpm for 10 min and an aliquot was removed from each centrifuge bottle for ICP analysis of As, Zn, Cu, Cr, Fe, Al, and Mn. The choice of desorbing agents and their replenishment were based on considerations reported elsewhere [20,21]. The desorbing agents were 0.01 M $CaCl_2$, 0.25 M Na_2HPO_4, or a 0.20 M $(NH_4)_2$-oxalate/0.10 M ascorbic acid. The $CaCl_2$ solution targets weakly bound or outer-sphere bound ions, the phosphate solution targets inner- and outer-sphere adsorbed AsO_4 species, and the oxalate/ascorbic acid solution (a strong reducing agent used to convert amorphous Fe^{3+} (s) to Fe^{2+} (aq) and form a chelate with ferrous iron) targets As associated with amorphous Fe (and possibly Al) phases. Similar experiments have been conducted by other researchers with similar treatments and evaluations of their effects [22–26]. Each treatment was carried out in triplicate with averaged results reported in Fig. 2.

2.3. μSXRF and μXAFS data collection

Synchrotron-based, micro-focused X-ray fluorescence (μSXRF) spectroscopy and micro-focused X-ray absorption fine structure (μXAFS) spectroscopy experiments were conducted at beamline 10.3.2 of the Advanced Light Source (Lawrence Berkeley National Laboratories, Berkley, CA); the beamline operation and configuration have been discussed elsewhere [27,28]. This beamline provides a monochromatic beam of hard X-rays whose spot size can be varied between 16×7 and 5×5 μm^2 (H $\times$ V). For μSXRF, the sample was scanned under this probe while fluorescent X-rays were monitored by a 7-element Canberra Ultra LE Ge detector. For μXAFS data collection, the energy was varied across the As K-edge, while the sample remained fixed in the beam path at a point of interest identified on a μXRF image. Energy calibration of the monochromator was done using an arsenate standard (Na_2HAsO_4, 10 wt% in BN, As(V) K-edge taken as 11.874 keV at the inflection point). The samples were investigated either as 30 μm
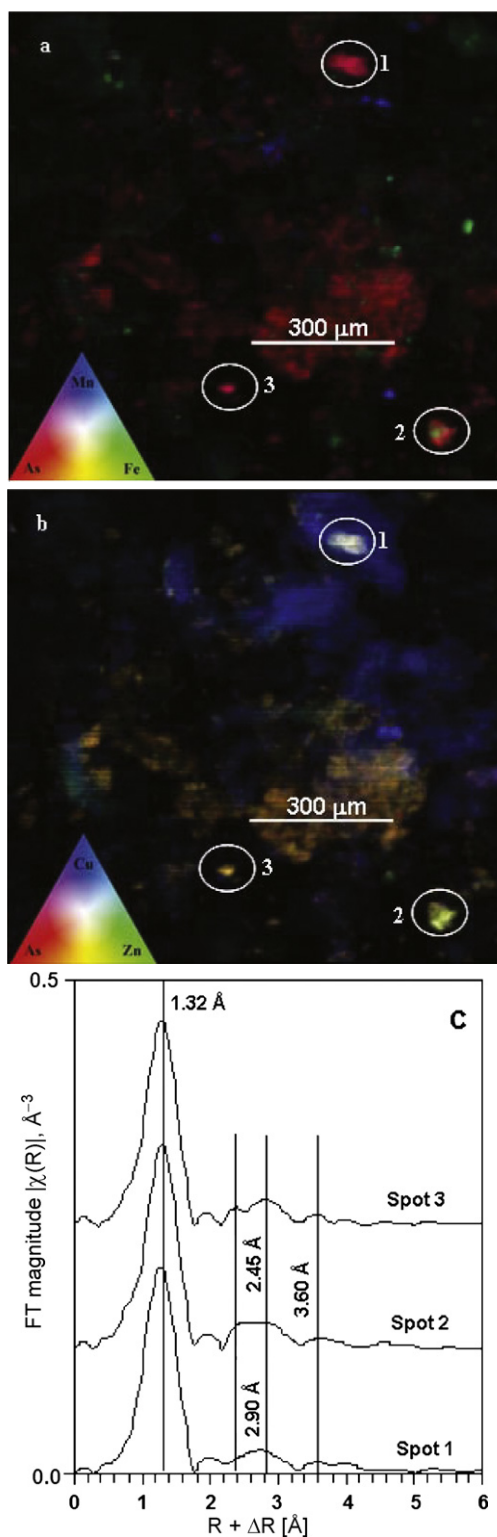
Fig. 3. μX-ray fluorescence images from LM-A Map C using an (a) AsMnFe and an (b) AsCuZn filter. Fourier transforms of spots marked 1–3 show a consistent position of the first ligand shell and low amplitude second and higher order shell peaks.

Fig. 4. μX-ray fluorescence images from LM-A TS Map 2 using an (a) AsMn-Fe and an (b) AsCuZn filter. Fourier transforms of spots marked 1–3 show a consistent position of the first ligand shell and low amplitude second and higher order shell peaks for Spots 2 and 3. The greater amplitude on Spot 1 suggests the possible presence of a precipitated As phase.

thin sections (embedded in 3M Scotchcast electrical resin), or as powder films on Kapton tape. Both size fractionated and un-fractionated powder samples were investigated. Size fractionated samples were obtained by settling a predefined amount
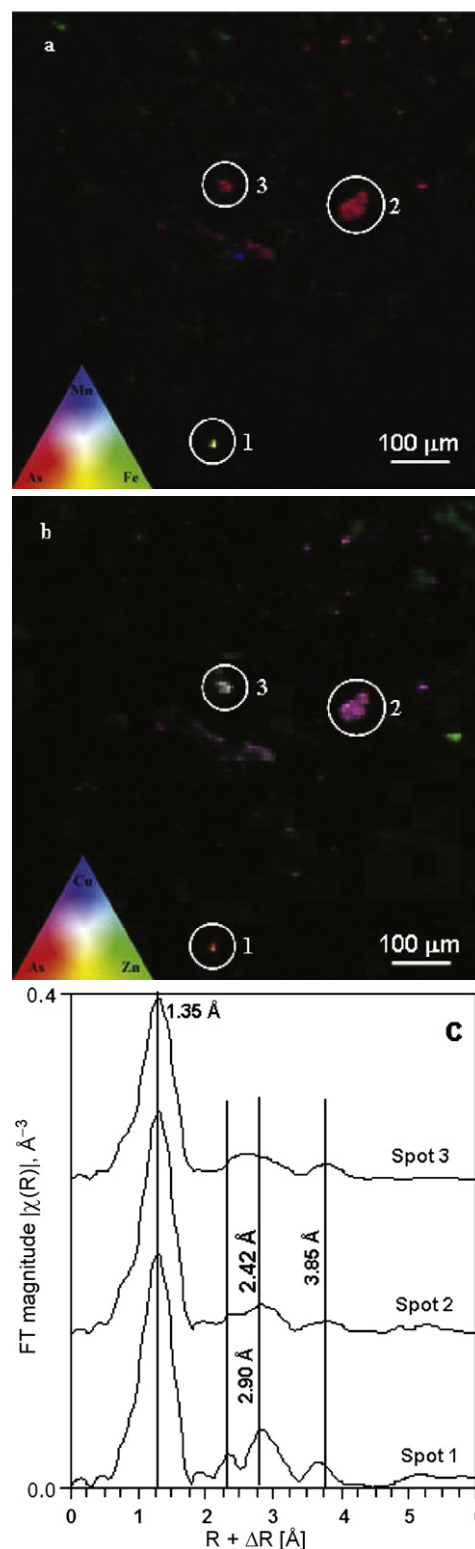
of soil in 80 mM sodium hexametaphophate for 2 h following standard procedures. A core of the settled out soil was then divided into three sections by visual inspection and freeze-dried:
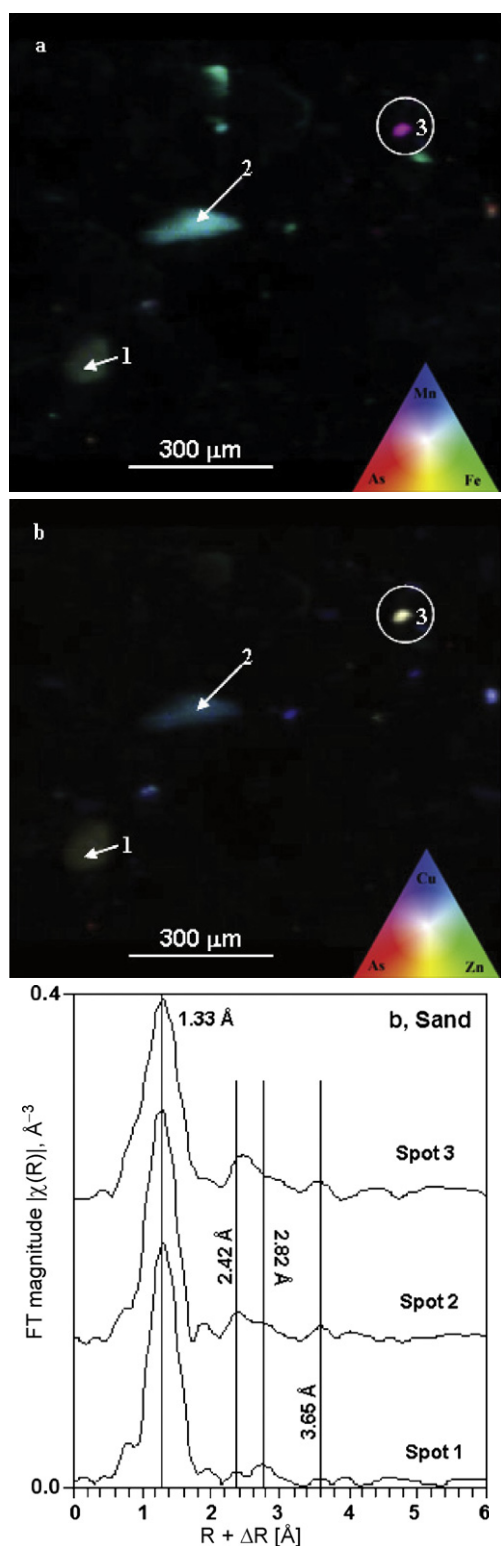
cence counts of As and other elements of interest (Figs. 3a, 3b, 4a, 4b, 5a, 5b, 6a, and 6c–6f). During a mapping run, the energy of the beam was set to mid range (12.224 keV) of the (subsequent) μXAFS experiment thereby enabling us to observe fluorescence signals of elements from potassium (K) to As. The fluorescence yields were normalized against the incident intensity (I_0) of the X-ray beam and the dwell time. Scatter plots of the fluorescence counts between two elements were derived from the fluorescence information contained in each pixel of each map, and a linear Pearson correlation coefficient (ρ) was calculated to evaluate the co-occurrence between two elements (Table 2, Fig. 6b). Between one and three suitable spots for As K-edge μXAFS spectroscopy were selected per map. Arsenic K-edge (11.874 keV) μXAFS data were recorded in triplicate from 200 eV below to 750 eV above the edge energy.

2.4. Data analysis

All data were initially analyzed using WinXAS 2.1 [29] software package. Individual spectra were background corrected and normalized prior to averaging. The abscissa were converted from energy to photoelectron wave vector units (k = wave vector number with units of $\sim$Å^{-1}) by assigning the origin, E_0, to the first inflection point of the absorption edge. A cubic spline function consisting of $\leqslant$seven knots was applied in a linear least-squares fit over an average range in k-space (ca. 2–13 Å^{-1}). Fourier transformation (FT) of the raw $k^3\chi(k)$ function was performed over a consistent region in k-space (2.50–12.75 Å^{-1}) and a radial structure function (RSF) was obtained using a Bessel window function ($\beta = 4$, see Figs. 3c, 4c, 5c, and 6g). From comparison of the second and higher order shell regions, RSF segments between 2.25 and 3.50 Å ($R + \Delta R$, uncorrected for phase shift) were Fourier back-transformed to k-space for linear least-square combination fitting against reference compounds [18]. Additional reference materials (denominated in Table 3 by superscript d) were collected at beamline 17C1 of the National Synchrotron Radiation Research Centre (NSSRC, Hsinchu—Taiwan). Details of this synchrotron facility and the beamline can be found elsewhere [30,31]. The spectra were collected with either a 13-element solid state detector (jaorsite and goethite-based samples) or a Kr gas purged Lytle detector (kaolinite and gibbsite-based samples). At least three scans per sample were collected and averaged. The data interpretation followed the same procedure as outlined in the companion paper to this publication.

2.5. Oxidation state analysis

The oxidation state of As in soil spectra was evaluated by comparing the position of the inflection point obtained from the first derivative of the absorption edge of soil XANES spectra. Hereby it was noticed, however, that all spectra (including bulk XAFS spectra) suffered from increasing radiation damage as observed from sequential shifts of the inflection point to lower energies. To quantify contributions to the spectra

Fig. 5. μX-ray fluorescence images from LM-B sand using an (a) AsMnFe and an (b) AsCuZn filter. Fourier transforms of spots marked 1–3 show a consistent position of the first ligand shell and low amplitude second and higher order shell peaks.

a sand only fraction (Sand), a sand-silt-clay mixture (SaSiCl), and a silt-clay fraction (SiCl).

Elemental maps were obtained by scanning successively smaller areas and regions of interest containing high fluores-
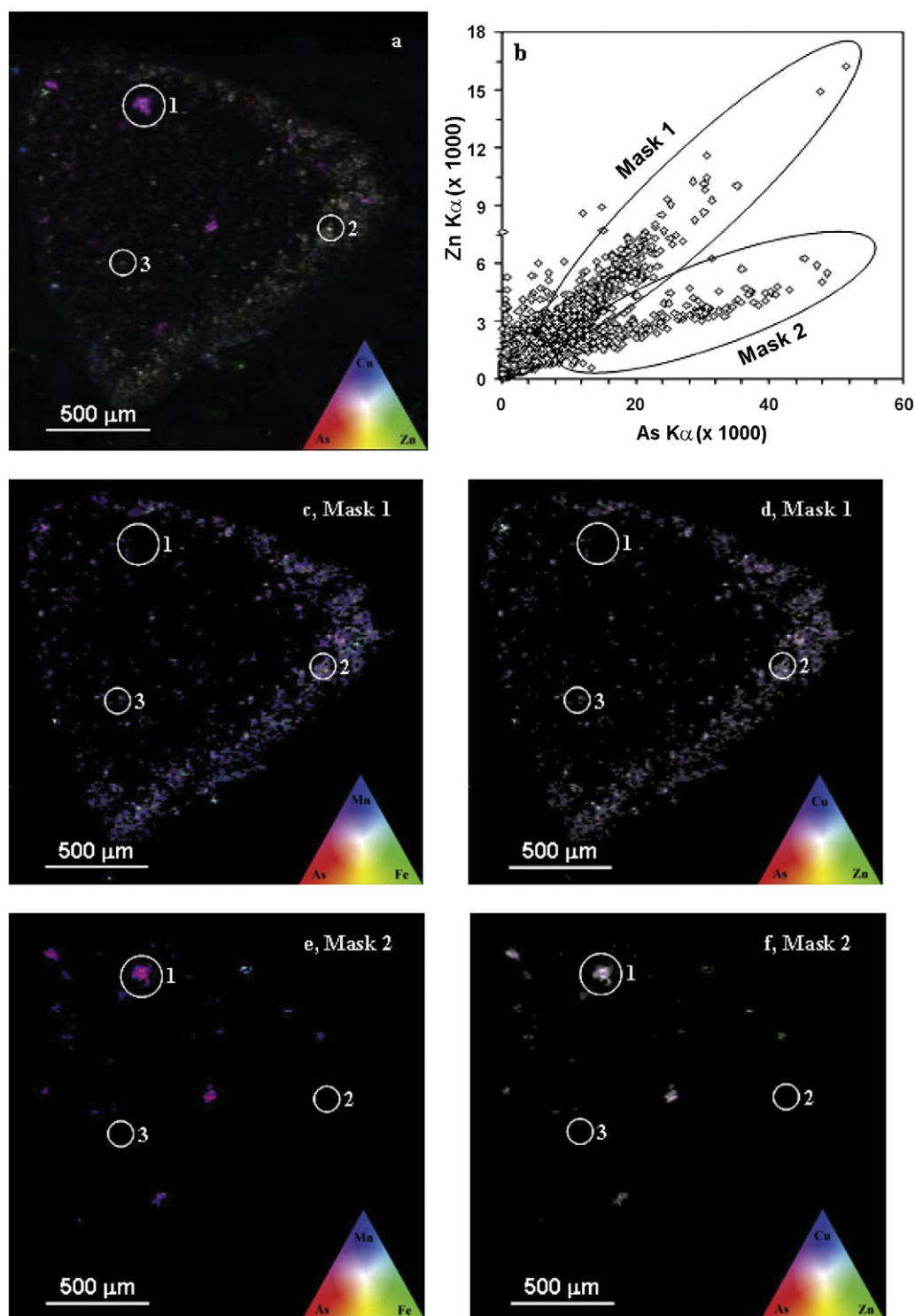
Fig. 6. μX-ray fluorescence images from LM-B TS Map 2 using an (a) AsCuZn filter [42]. (b) The scatter plot between As and Zn counts suggests two regions of As and Zn accumulation on the fluorescence map. (c and d) μX-ray fluorescence images of Mask 1 pixels using an AsMnFe and an AsCuZn filter identify Spot 1, whereas (e and f) μX-ray fluorescence images of Mask 2 pixels using an AsMnFe and an AsCuZn filter identify Spots 2 and 3. (g) Fourier transforms of spots marked 1–3 show a consistent position of the first ligand shell. The amplitude of the second shell moduli of Spots 1 and 3 suggest precipitated As phases.

from arsenite (H_3AsO_3) and sulfur-coordinated arsenic atoms (e.g., As_2S_3), the first peak in the RSF, due to first ligand shell backscattering, was Fourier back-transformed and linearly fitted with a combination of As–O and As–S backscattering atoms extracted from RSFs of Na_2HAsO_4, H_3AsO_3, and As_2S_3 reference spectra using beamline 10.3.2's linear combination fitting program (data analysis software available at http://xraysweb.lbl.gov/uxas/Index.htm). The inclusion of more than one fit component (i.e., oxidation state) required an improvement of the linear fit by 20 percent.

Table 2

Matrices comparing elemental Pearson correlations (ρ) in maps from thin sections (TS) for LM-A and LM-B

| TS Map 1						TS Map 2						TS Map 3						
	As	Cr	Cu	Fe	Mn	Zn	As	Cr	Cu	Fe	Mn	Zn	As	Cr	Cu	Fe	Mn	Zn	
									LM-A										
As		0.91	0.35	0.23	0.60	0.88		0.89	0.66	0.44	0.72	0.95		0.87	0.56	0.33	0.50	0.91	As
Cr	0.91		0.42	0.30	0.68	0.85	0.89		0.66	0.39	0.78	0.91	0.87		0.53	0.33	0.57	0.80	Cr
Cu	0.35	0.42		0.35	0.44	0.57	0.66	0.66		0.48	0.63	0.71	0.56	0.53		0.61	0.61	0.70	Cu
Fe	0.23	0.30	0.35		0.67	0.44	0.44	0.39	0.48		0.57	0.44	0.33	0.33	0.61		0.61	0.55	Fe
Mn	0.60	0.68	0.44	0.67		0.70	0.72	0.78	0.63	0.57		0.76	0.50	0.57	0.61	0.61		0.63	Mn
Zn	0.88	0.85	0.57	0.44	0.70		0.95	0.91	0.71	0.44	0.76		0.91	0.80	0.70	0.55	0.63		Zn
									LM-B										
As		0.80	0.63	0.70	0.60	0.93		0.49	0.96	0.27	0.28	0.78		0.75	0.71	0.15	0.28	0.72	As
Cr	0.80		0.63	0.58	0.58	0.76	0.49		0.43	0.65	0.55	0.55	0.75		0.55	0.13	0.32	0.55	Cr
Cu	0.63	0.63		0.55	0.52	0.68	0.96	0.43		0.24	0.24	0.73	0.71	0.55		0.16	0.23	0.54	Cu
Fe	0.70	0.58	0.55		0.67	0.68	0.27	0.65	0.24		0.78	0.39	0.15	0.13	0.16		0.16	0.14	Fe
Mn	0.60	0.58	0.52	0.67		0.59	0.28	0.55	0.24	0.78		0.36	0.28	0.32	0.23	0.16		0.22	Mn
Zn	0.93	0.76	0.68	0.68	0.59		0.78	0.55	0.73	0.39	0.36		0.72	0.55	0.54	0.14	0.22		Zn
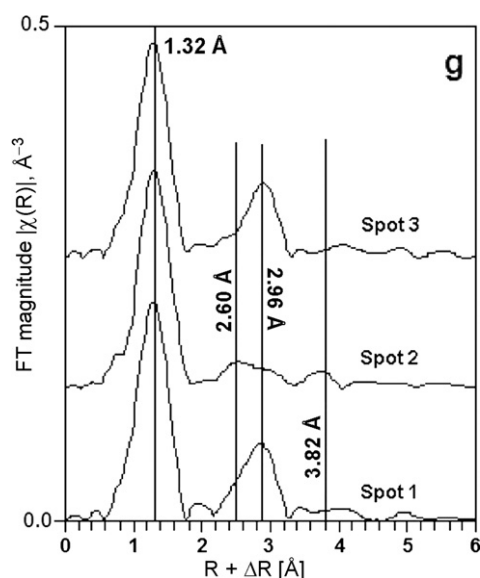
Fig. 6. (*continued*)

2.6. Abstract factor analysis (AFA)

Abstract factor analysis (also known as principal component analysis) as a means to describe large data [26,27,32,33] was conducted on k^3-weighted $\chi(k)$ spectra (2.50–12.75 Å) obtained after Fourier back-transforming a segment of the RSFs between 2.25 and 3.50 Å ($R + \Delta R$, uncorrected for phase shift) to k-space. In total, 31 spectra were analyzed [LM-A ($n = 14$) and LM-B ($n = 17$)] using beamline 10.3.2 Principal Component Analysis software (Table 4). This procedure involved the reproduction of the data set (LM-A and LM-B) using abstract (mathematical, nonphysical) factors, in which data points of experimental functions were reproduced as linear sums of product functions (i.e., the abstract factors) [34]. Principal component analysis (PCA) determines the number of abstract functions required to describe the complete set of experimental spectra (Figs. 7a–7c). Subsequently, target transformation analysis was conducted to characterize the selected principal components (PCs) (Table 3). Target transformation entails testing a known reference spectrum by removing from it all signals that cannot be described as a linear combination of the factors. The degree to which this operation alters the original reference spectrum is measured by a SPOIL value [27,35]. A high SPOIL indicates that the reference being tested cannot be described as a sum of the factors and is therefore not a plausible component of the experimental data. Meaningful SPOIL values range between 0 and 4.5 and were subdivided into quality criteria of excellent ($0 \leqslant \text{SPOIL} < 1.5$), good ($1.5 \leqslant \text{SPOIL} < 3$), and fair ($3 \leqslant \text{SPOIL} < 4.5$) (*ibid.*). Target analysis was performed using two and three principal components, comparing references meeting SPOIL $\leqslant 4.5$ and comparing SPOIL values for each reference phase as a function of the number of principal components used in the transformation. Degenerate reference spectra with higher SPOIL values were eliminated, thus consolidating a list of possible reference spectra for linear least-square combination fit analysis (LLSF, Table 3).

2.7. Linear least-square combination fitting (LLSF)

Linear least-squares combination fit analyses (LLSF) were conducted to reveal the composition of individual spectra using beamline 10.3.2's linear combination fitting program. The goodness-of-fit was evaluated by calculating a normalized sum-square value of the fit involving the inclusion of the ith component. In order for a second and third component/reference spectrum to be considered, the fit had to improve by at least 20 percent [27]. Examples of the LLSF analysis for bulk LM-A and LM-B spectra are presented in Figs. 8 and 11, respectively, and selected μEXAFS spectra (RSFs shown in Figs. 3–6) are presented in Figs. 9 and 10 (LM-A) and Figs. 11 and 12 (LM-B). The complete LLSF analysis is presented in Tables 5 and 6.

3. Results

3.1. Soil characterization

The investigated soil originated from an Arredondo–urban land complex with a taxonomic classification of a loamy,

Table 3
Summary of the target analyses with two PCs including a brief description of the reaction conditions and the As(V) bonding environment in each reference material or sorption standard

SPOIL	Reference	Sorbent	pH	Equil. period	Γ_{As}[a]	$\Gamma_{Cu, Zn}$[a]	As–M, MS	CN	R (Å)
0.99	AsCuZnCr$_2$O$_3$[b]	α-Cr$_2$O$_3$	7.00	24 h			As–Cu(#C)	4.2	3.21
							As–Cu/Zn(#C)	1.1	3.39
1.04	AsCuCr$_2$O$_3$[b]	α-Cr$_2$O$_3$	7.00	24 h			As–Cu(#C)	8.1	3.23
							As–Cu(#C)	3.2	3.42
1.71	Scorodite[b]	n/a	n/a	n/a	n/a	n/a	As–Fe(1C)	4.6	3.33
1.95	$^{2\,w}$AsZnGoe$_{10\,ppm}$[c]	Goethite	7.00	14 d	115.7	184.5	MS	9.9	3.08
							As–Zn(2C)	2.6	3.28
2.29	$^{12\,d}$As$_1$Cu$_5$Goe$_{141\,ppm}$[d]	Goethite	5.65	12 d	1.5	2.9	MS	12.3	3.09
							As–Cu(#C)	1.2	3.23
							As–Cu(#C)	0.5	3.38
2.5	$^{24\,h}$AsCuGoe$_{1000\,ppm}$[b]	Goethite	7.00	24 h	1.9	4.3	MS	12.1	3.11
							As–Cu/Fe(1E)	0.4	2.85
							As–Cu/Fe(2C)	2.1	3.29
2.53	CuZnAsPrecip[b]	n/a	7.00	24 h			As–Cu(#C)	3.9	3.22
							As–Cu/Zn	1.1	3.38
2.55	$^{12\,d}$As$_1$Cu$_{10}$Jar$_{2940\,ppm}$[d]	Jarosite	5.65	12 d	0.8	9.5	MS	12.3	3.09
							As–Cu/Fe(1E)	0.3	2.78
							As–Cu(#C)	1.2	3.23
							As–Cu(#C)	0.5	3.38
2.57	$^{24\,h}$AsCuZnGib$_{1000\,ppm}$[b]	Gibbsite	7.00	24 h	2.4	4.3, 3.2	MS	12.3	3.09
							As–Cu(1E)	0.3	2.82
							As–Cu/Zn(#C)	1.6	3.25
2.58	$^{24\,h}$As$_{0.75}$Zn$_{0.75}$Goe$_{1000\,ppm}$[e]	Goethite	7.00	24 h	3.8	3.6	As–Fe/Zn	2.5	3.29
							As–Zn	2.2	3.44
2.69	CuAsPrecip[b]	n/a	7.00	24 h			As–Cu(# C)	5.6	3.23
							As–Cu(#C)	2.4	3.39
2.81	$^{24\,h}$AsCuGib$_{1000\,ppm}$[b]	Gibbsite	7.00	24 h	2.4	5.6	MS	12.3	3.10
							As–Cu(1E)	0.3	2.82
							As–Cu(#C)	1.6	3.23
2.84	$^{24\,h}$AsCuZnGoe$_{1000\,ppm}$[b]	Goethite	7.00	24 h	2.7	4.2, 2.9	MS	10.9	3.11
							As–Fe/Cu/Zn(1E)	0.3	2.84
							As–Fe/Zn	1.6	3.28
2.94	Adamite[b]	n/a	n/a	n/a	n/a	n/a	MS	14.0	3.19
							As–Zn(#C)	6.4	3.37
3.17	$^{12\,d}$As$_1$Cu$_{10}$Goe$_{141\,ppm}$[d]	Goethite	5.65	12 d	1.9	4.1	MS	12.3	3.09
							As–Fe/Cu(1E)	0.3	2.78
							As–Cu(#C)	1.2	3.23
							As–Cu(#C)	0.5	3.38
3.17	Chalcophyllite[b]	n/a	n/a	n/a	n/a	n/a	As–Cu(#C)	5.4	3.32
3.32	$^{24\,h}$AsZnGoe$_{10\,ppm}$[c]	Goethite	7.00	24 h	12.2	48.6	MS	11.0	3.16
							As–Fe/Zn(2C)	2.0	3.28
3.56	$^{24\,h}$As$_{0.25}$Zn$_{0.25}$Goe$_{1000\,ppm}$[e]	Goethite	7.00	24 h	1.1	1.3	As–Fe/Zn(2C)	1.2	3.27
							As–Fe/Zn(1C)	0.9	3.43
3.58	$^{24\,h}$As$_{2.5}$Zn$_{2.5}$Goe$_{1000\,ppm}$[e]	Goethite	7.00	24 h	13.2	13.8	As–Zn(#C)	5.9	3.34
3.6	$^{4\,w}$AsZnGoe$_{1000\,ppm}$[c]	Goethite	7.00	30 d	2.5	3.0	MS	16.9	3.22
							As–Fe/Zn(1E)	0.6	2.80
							As–Fe/Zn(2C)	1.8	3.31
3.62	Ojuelaite[b]	n/a	n/a	n/a	n/a	n/a	MS	17.0	3.16
							As–Fe/Zn(1E)	0.9	2.77
							As–Fe/Zn(2C)	2.5	3.34
3.63	$^{24\,h}$As$_{0.5}$Goe$_{1000\,ppm}$[e]	Goethite	7.00	24 h	1.24	n/a	MS	12.6	3.11
							As–Fe(1E)	0.2	2.87
							As–Fe(2C)	1.7	3.28
3.67	$^{24\,h}$AsZnGoe$_{100\,ppm}$[c]	Goethite	7.00	24 h	3.3	11.3	MS	13.6	3.20
							As–Fe/Zn(#C)	3.6	3.31
3.78	$^{24\,h}$As$_1$Cu$_5$Jar$_{2940\,ppm}$[d]	Jarosite	5.65	12 d	4.4	24.8	MS	13.8	3.09
							As–Fe/Cu(1E)	0.3	2.89
							As–Cu(#C)	0.9	3.17
							As–Cu(#C)	1.6	3.31
							As–Cu(#C)	1.5	3.86

Table 3 (continued)

SPOIL	Reference	Sorbent	pH	Equil. period	Γ_{As}[a]	$\Gamma_{Cu,Zn}$[a]	As–M, MS	CN	R (Å)
3.86	[24 h]$As_{0.25}Goe_{1000\ ppm}$[e]	Goethite	7.00	24 h	1.0	n/a	As–Fe(2C)	1.5	3.28
							As–Fe(1C)	0.8	3.47
3.87	[12 d]$As_1Cu_{25}Goe_{141\ ppm}$[d]	Goethite	5.65	12 d	1.0	3.8	MS	13.0	3.11
							As–Fe/Cu(1E)	0.2	2.87
							As–Cu(#C)	1.0	3.20
							As–Cu/Fe(2C)	1.2	3.32
3.97	Olivenite[b]	n/a	n/a	n/a	n/a	n/a	As–Cu(#C)	5.5	3.26
							As–Cu(#C)	1.2	3.47
4.07	[4 w]$AsGoe_{1000\ ppm}$[c]	Goethite	7.00	30 d	2.2	n/a	MS	18.7	3.23
							As–Fe(1E)	0.5	2.80
							As–Fe(2C)	2.0	3.32
4.21	[6 mo]$AsZnGoe_{100\ ppm}$[c]	Goethite	7.00	6 mo	20.5	34.3	MS	11.7	3.11
							As–Zn(#C)	6.9	3.34
4.42	[24 h]$AsGib_{1000\ ppm}$[b]	Gibbsite	7.00	24 h	1.0	n/a	MS	18.0	3.11
							As–Al(1E)	0.4	2.72
							As–Al(2C)	1.6	3.17
4.50	[12 d]$AsJar_{2940\ ppm}$[d]	Jarosite	5.50	12 d	13.6	n/a	MS	14.0	3.03
							As–Fe(1E)	0.9	2.86
							As–Fe(2C)	2.3	3.22

[a] $\Gamma_{As,Cu,Zn}$ = surface loading in $\mu mol\ m^{-2}$.

[b] For greater detail see [18].

[c] For greater detail see [13].

[d] This study: samples collected at beamline 17C1 of the NSRRC using either a Kr-gas purged Lytle detector or a 13-element Ge solid state detector.

[e] For greater detail see [12].

Table 4
Principal component analysis of 29 μXAFS and 2 bulk XAFS ($k^3\chi(k)$) spectra following Fourier filtering of 2.25 to 3.50 Å ($R + \Delta R$) from LM-A and LM-B

PC#[a]	Eigenvalue	% Δ eigenvalue[b]	IND[c]	NSS (tot.)[d]	% Δ NSS (tot.)[e]	Incl.
				1		
1	63.7		0.0102	0.3820	61.8	x
2	39.9	37.4	0.0067	0.1400	63.4	x
3	20.9	47.6	0.0053	0.0736	47.4	
4	15.2	27.3	0.0042	0.0385	47.7	
5	11.0	27.6	0.0033	0.0200	48.1	
6	7.8	29.3	0.0027	0.0108	46.0	
7	6.4	17.2	0.0019	0.0045	58.1	
8	4.4	32.5	0.0013	0.0016	63.7	
9	2.5	43.2	0.0010	0.0007	56.4	
10	2.1	14.6	0.0002	0.0000	94.6	

[a] PC# = principal component number.

[b] % Δ eigenvalue = ([(eigenvalue)$_i$ − (eigenvalue)$_{ii}$]/(eigenvalue)$_i$) × 100.

[c] IND = Malinowski indicator value.

[d] NSS (tot.) = normalized sum-square = $\sum((y - y_{fit})^2)/\sum(y^2)$, total refers to the sum of all points in all spectra.

[e] % Δ NSS (tot.) = ([(NSS(tot))$_i$ − (NSS(tot.))$_{ii}$]/(NSS(tot))$_i$) × 100.

siliceous, hyperthermic Grossarenic Paleudult [36]. Across the upper 40 cm, *circa* 85 percent of the soil consists of sand-sized, 12 percent of silt-sized, and three percent of clay-sized particles (Table 1). Bulk-XRD analysis revealed that quartz and kaolinite were the dominant crystalline soil components, and the presence of micro-crystalline goethite and gibbsite was suggested by low intensity peaks (Fig. 1a). The mineral composition and low organic matter content (2.9 vs 1.2 weight percent; LM-A and LM-B, respectively) reflect a low cation exchange capacity (CEC) of the soil (Table 1). The CEC (pH 7, 10 vs 6 meq$_c$ 100 g^{-1} soil, LM-A and LM-B, respectively) was directly related to the low OM content, which dropped similarly by half from LM-A to LM-B. *Circa* 1300 mg kg^{-1}

(ppm) Cu, 450 ppm Cr, and 880 ppm As were found in LM-A (Fig. 1b). Concentrations of Cu, Cr, and As were about 75 percent lower in LM-B than in LM-A. Total acid digests of the soil fractions revealed that the soil also contained 700 ppm Zn in LM-A and 170 ppm Zn in LM-B. The Fe content in LM-A (14.6 ppt) dropped by 87 percent (1.8 ppt) in LM-B. In contrast, the Al content (5.5 ppt in LM-A and 3.8 ppt in LM-B) was more comparable with depth. The Mn content was less than 100 ppm throughout the entire soil suggesting that the XRD peak at ca. 24° 2θ was mostly due to kaolinite and not birnessite (δ-MnO_2). The soil solution pH was between 7.0 and 7.5 as a result of $CaCO_3$ applications to the site.
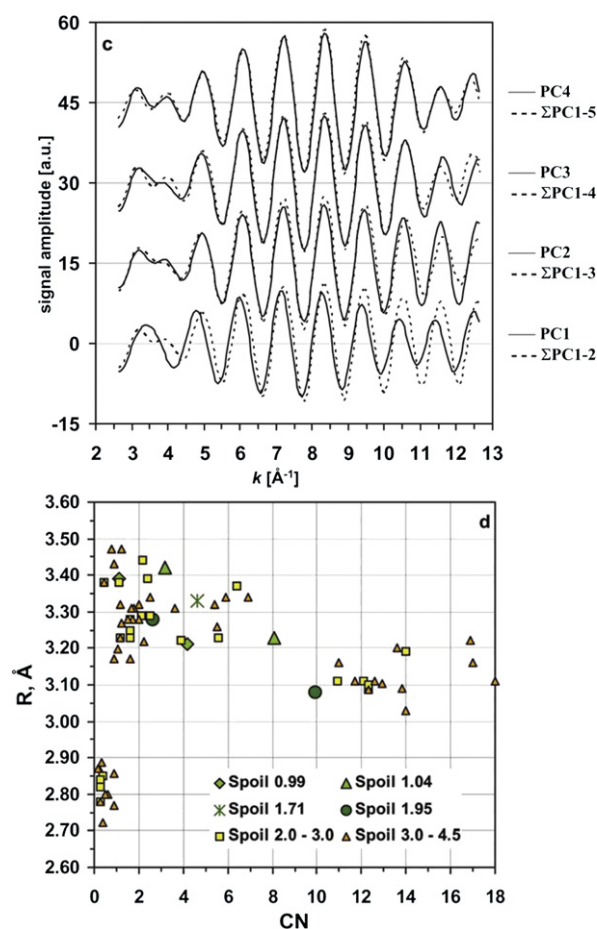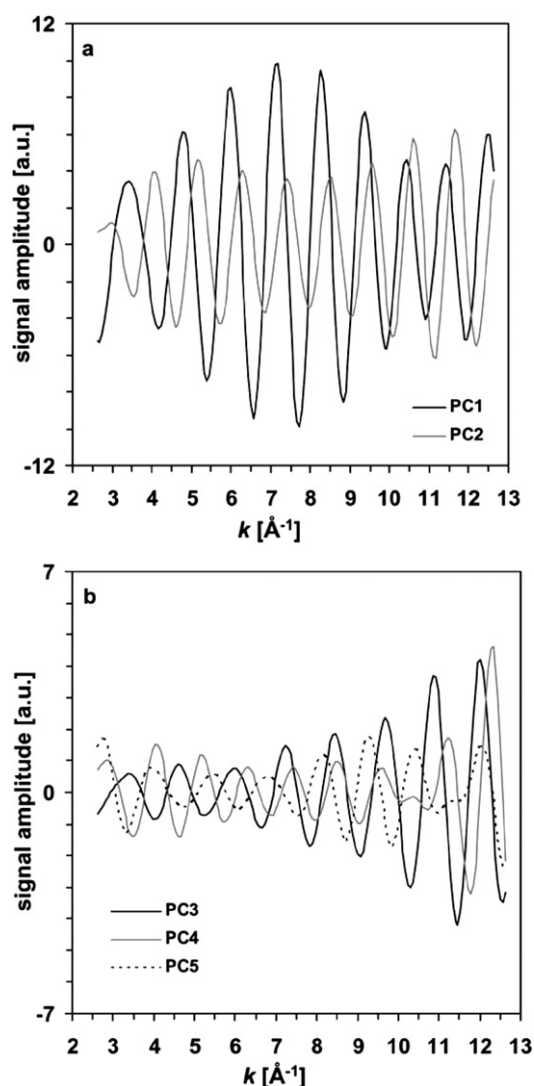
Fig. 7. Principal components of 29 μXAFS and 2 bulk XAFS ($k^3\chi(k)$) spectra following Fourier filtering of 2.25 to 3.50 Å ($R + \Delta R$) from LM-A and LM-B: (a) PC1 and PC2, (b) PC 3 to 5, and (c) co-added PCs as indicated. (d) Scatter plot of coordination number (CN) versus radial distance (R) for the reference phases identified with target analysis. Points with CN < 1 and $R \sim 2.80$ Å are edge-sharing coordinates, points with CN > 10 and $R \sim 3.10$ Å are multiple scattering coordinates. The coordinates of reference phases with low SPOIL values show 4 to 8 metal neighbors near 3.2 and 1 to 3 metal neighbors near 3.4 Å. With increasing SPOIL value the coordinates shift toward lower CN suggesting an increasing number of adsorption complexes rather than poorly ordered precipitates or fully precipitated phases.

Fig. 7. (*continued*)

3.2. Replenishment desorption study

Arsenic, Cu, Cr, Fe, Al, Mn, and Zn desorbed increasingly from soils in LM-A and LM-B with increasing aggressiveness of the desorbing agents (Fig. 2). The lability of As, Cu, and Zn was generally greater in LM-B than in LM-A. Zinc was the most labile ion and was almost completely removed in the oxalate/ascorbic acid treatment from LM-A and LM-B after the application of 6 pore volumes. The CaCl$_2$ solution removed less than 5 percent As from the soil surface, whereas Na$_2$HPO$_4$ removed *circa* 50 percent As from the soil, suggesting that As was bound primarily as inner-rather than outer-sphere complexes.

The combination of NH$_4$-oxalate/ascorbic acid removed ca. 90 percent As from the soil and corroborated inner-sphere complexation of As. An increase of Fe and Al in solution suggested that Al and Fe bearing solid phases were dissolving during this treatment possibly contributing to the increased release of As, Zn, Cr, and Cu.

3.3. μSXRF

Micro X-ray fluorescence (μSXRF) images taken from thin-sectioned and powder-on-tape samples from the 0–20 (LM-A) and 20–40 (LM-B) cm depth fractions showed strong co-localization of As with Cr, Mn, Cu, and Zn and to a lesser degree with Fe. Pearson correlations (ρ) between elements were determined only from maps of thin-sectioned samples to minimize false-positive correlations, i.e., thickness effects induced from radially displaced particles prominent in some powder-on-tape samples. Between 0–20 cm, As correlated decreasingly to Cr $\approx$ Zn $\gg$ Cu $\approx$ Mn > Fe (Table 2). Arsenic–Cr and As–Zn correlations were $\geqslant$ 0.80 throughout the upper 20 cm of soil. In contrast, ρ_{As-Cu} was only 0.56 and ρ_{As-Fe} was only 0.33. Surprisingly, ρ_{As-Mn} of 0.60 was similar to that of As–Cu and *circa* twice as high as ρ_{As-Fe}. The correlation of Mn to Cr, Cu and Zn was on average 0.68 ranging between 0.44 (Cu) and 0.78 (Cr), suggesting that the high correlation between As and Mn in LM-A may have been due to the presence of these metals.
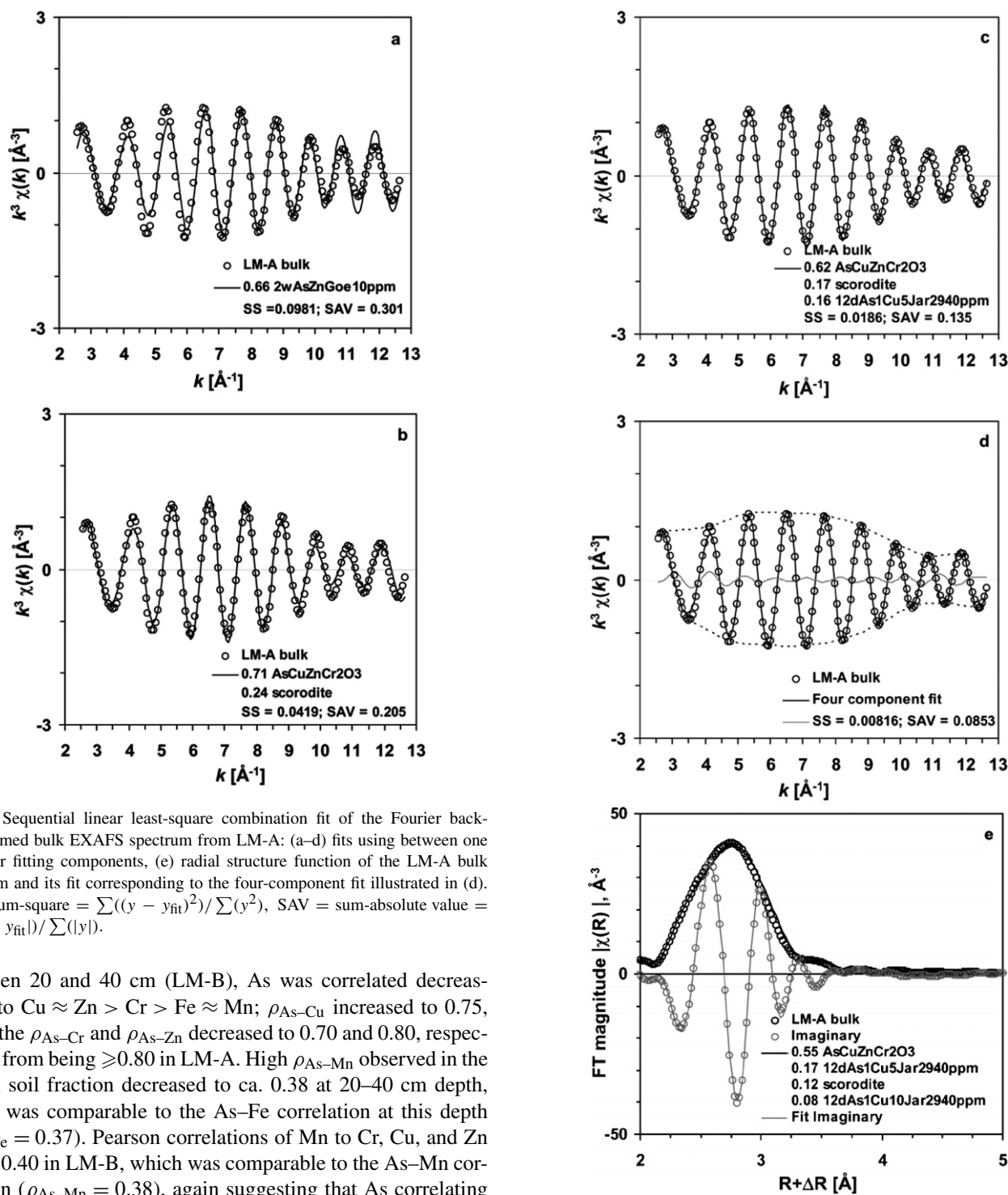
Fig. 8. Sequential linear least-square combination fit of the Fourier back-transformed bulk EXAFS spectrum from LM-A: (a–d) fits using between one and four fitting components, (e) radial structure function of the LM-A bulk spectrum and its fit corresponding to the four-component fit illustrated in (d). SS = sum-square = $\sum((y - y_{fit})^2)/\sum(y^2)$, SAV = sum-absolute value = $\sum(|y - y_{fit}|)/\sum(|y|)$.

Between 20 and 40 cm (LM-B), As was correlated decreasingly to Cu ≈ Zn > Cr > Fe ≈ Mn; $\rho_{As–Cu}$ increased to 0.75, while the $\rho_{As–Cr}$ and $\rho_{As–Zn}$ decreased to 0.70 and 0.80, respectively, from being ⩾0.80 in LM-A. High $\rho_{As–Mn}$ observed in the LM-A soil fraction decreased to ca. 0.38 at 20–40 cm depth, which was comparable to the As–Fe correlation at this depth ($\rho_{As–Fe} = 0.37$). Pearson correlations of Mn to Cr, Cu, and Zn fell to 0.40 in LM-B, which was comparable to the As–Mn correlation ($\rho_{As–Mn} = 0.38$), again suggesting that As correlating to Mn may have been by association with one or all of these metal cations.

On thin-sections and powder-on-tape samples alike, the fluorescence intensity from As was not uniform over any area, but rather, increased in discrete areas often not larger than 50 μm in diameter, suggesting that As accumulated preferentially in some areas over others. In such discrete areas, $\rho_{As–Cr, Cu, Fe, Mn, and Zn}$ exceeded 0.80 indicating strong positive co-localization of the co-contaminating metal cations in regions of As accumulation. Such areas could indicate the presence of co-precipitates or conversely an area of high surface

Fig. 8. (*continued*)

site availability such as an amorphous Fe, Mn, or Al hydroxide allowing As, Cu, Zn, and Cr to adsorb (Figs. 3–6). The presence of precipitates was suggested in some cases by the increased amplitudes of the Fourier transform (FT) magnitude in the RSFs between 2 and 4 Å ($R + \Delta R$, uncorrected for phase shift), whereas in many other cases, the magnitude of the FT peaks over the same range suggested surface adsorption complexes. Identifying variability among areas of As accumulation was achieved by masking and replotting linear elemental corre-
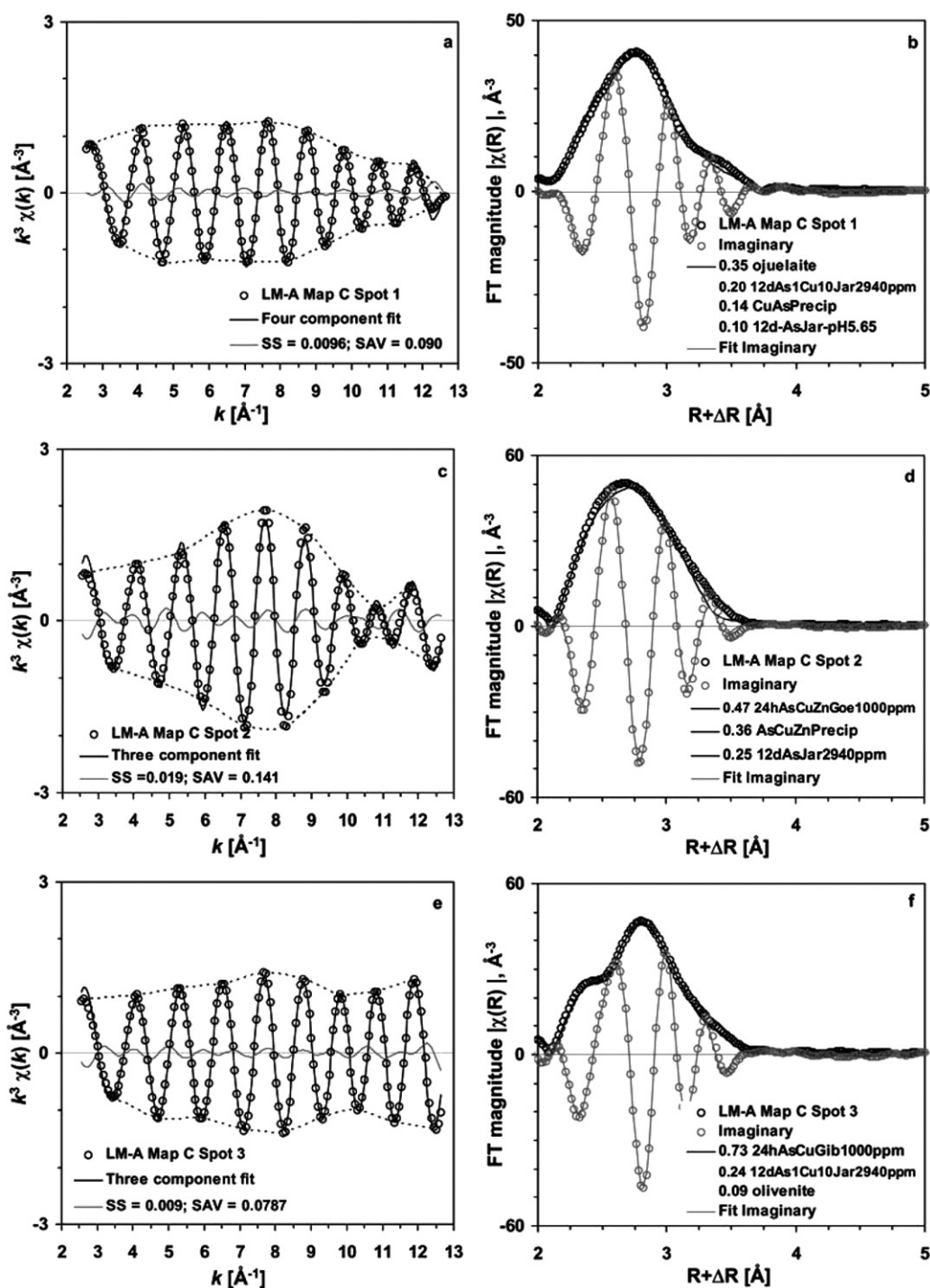
Fig. 9. Linear combination fit of Spots 1, 2, and 3 on LM-A Map C (Figs. 3a and 3b) showing the fitted k^3-weighted $\chi(k)$ function (a, c, and e) and the corresponding RSFs (b, d, and f). The dashed lines in (a), (c), and (e) outline the absorption envelope of each experimental spectrum.

lations of varying slopes in scatter-plots of fluorescence signal between two elements (e.g., Figs. 6a–6f). In this way, diversity among As hot and softspots was achieved and thus could be further investigated with μXAFS spectroscopy (Fig. 6g).

3.4. Oxidation state

The oxidation state of arsenic in the soil was predominantly (>96 percent) 5+, indicating the presence of As(V). This ob-

servation was supported by linear combination fits of isolated and Fourier back-transformed first ligand shells, and was in good agreement with the soil's physical characteristics (sandy texture, a lack of inundated conditions and a well-aerated soil profile). Linear combination fits of isolated and Fourier back-transformed first ligand shells indicated that at most 5 and 3 percent As(III) and As_2S_3 (orpiment), respectively, were present in LM-A and LM-B. However, reduction of As(V) to As(III) could have been an artifact of the irradiation by X-rays across
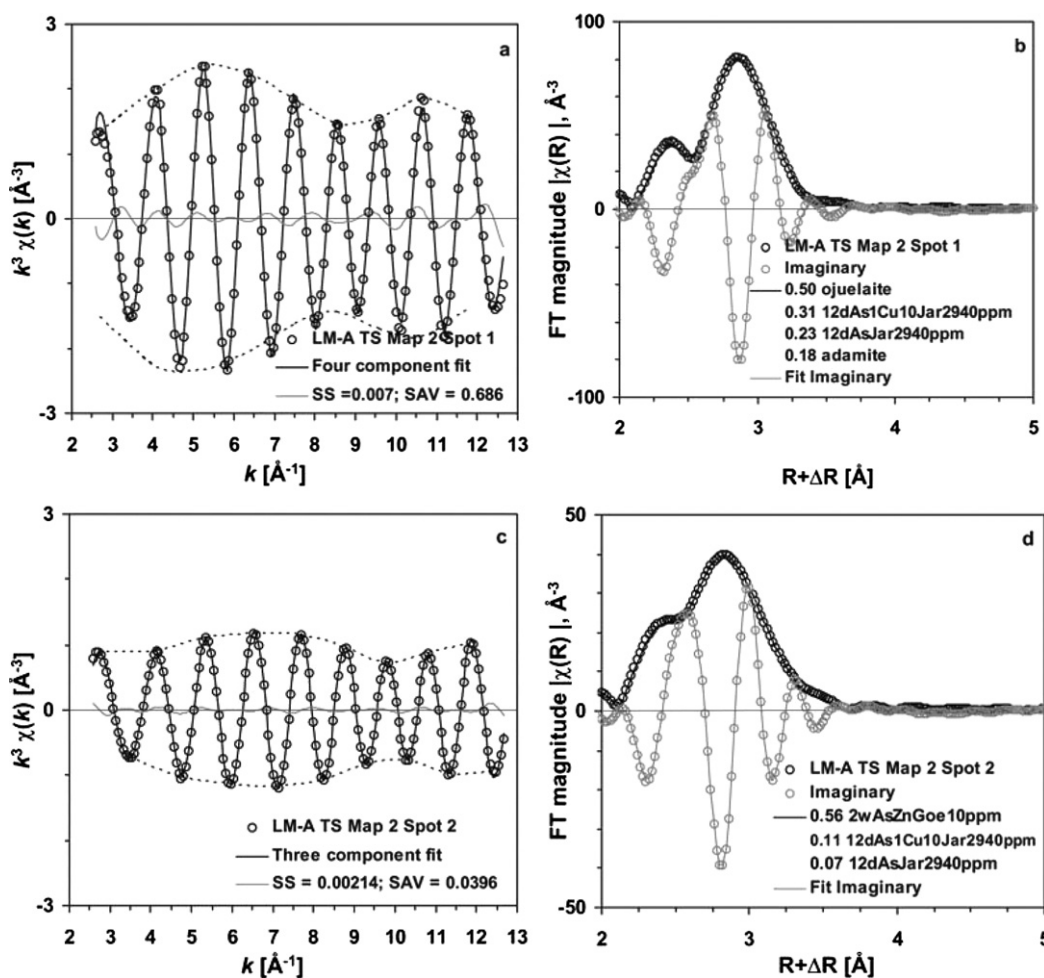
Fig. 10. Linear combination fit of Spots 1 and 2 on LM-A TS Map 2 (Figs. 4a and 4b) showing the fitted k^3-weighted $\chi(k)$ function (a and c) and the corresponding RSFs (b and d). The dashed lines in (a) and (c) outline the absorption envelope of each experimental spectrum.

the As K-edge, which is known to induce photo-reduction at times. This was indeed observed for the two bulk spectra of LM-A and LM-B, whose edge-jumps successively decreased in energy with repeat scans despite being mounted with adhesive-free Mylar films. The inflection point of the absorption edge for As(V) has been measured at ca. 11.874 keV [37], but the inflection point in the μXAFS spectra consistently occurred between 11.870 and 11.872 keV, suggesting photo-reduction of As in the X-ray beam.

3.5. Abstract factor analysis

Abstract factor analysis and linear least-square combination fit analyses were conducted after Fourier-filtering 2.25 to 3.50 Å from each of the experimental RSFs to k-space and k^3-weighting each $\chi(k)$ spectrum. The minimum number of principal components (PCs) required for reproducing the 31-spectra data set could not be assessed from the IND criterion [34], because no local minimum within the first 10 PCs was observed. Visual inspection of the PCs (Figs. 7a and 7b) showed that signal amplitudes of PCs 3–5 were 2–6 times lower than that of PCs 1 and 2, reflecting the diminishing contributions from successive components to the co-added PC spectrum (Fig. 7c). We

calculated the marginal improvements of the total goodness of fit (NSS-tot., Table 4) to note how each successive PC improved the NSS (tot.) and observed that PCs 1 and 2 improved the fit equally by *circa* 62–63 percent, whereas PC3 and subsequent PCs improved the fit by only 47 percent. Target analysis for reference phases ($n = 52$) conducted with two and three selected PCs showed that the list of likely As solid phases remained unchanged with the inclusion of PC3, but decreased their SPOIL values. This corroborated the effect observed from co-adding PCs 1–3 (Fig. 7c) that PCs at and above 3 were not significant.

Target analysis from transformations using two principal components showed that the excellent criterion (SPOIL < 1.5) was met by $CuAsCr_2O_3$ and $CuZnAsCr_2O_3$, two copper-arsenate precipitates with and without structural Zn conforming to the average bonding environments of clinoclase [38]. These two copper-arsenate species have a similar distribution of metal atoms around As at *circa* 3.2 and 3.4 Å, but the associated CN numbers are *circa* twice as high in the Zn-free, $CuAsCr_2O_3$ precipitate (Fig. 7d, Table 3). The magnitude of the coordination numbers and the distribution of metal cations around As(V) suggest that the nature of As(V) species in the data set overall are precipitated or poorly ordered precipitated species. Scorodite and a precipitated zinc-arsenate phase on goethite,
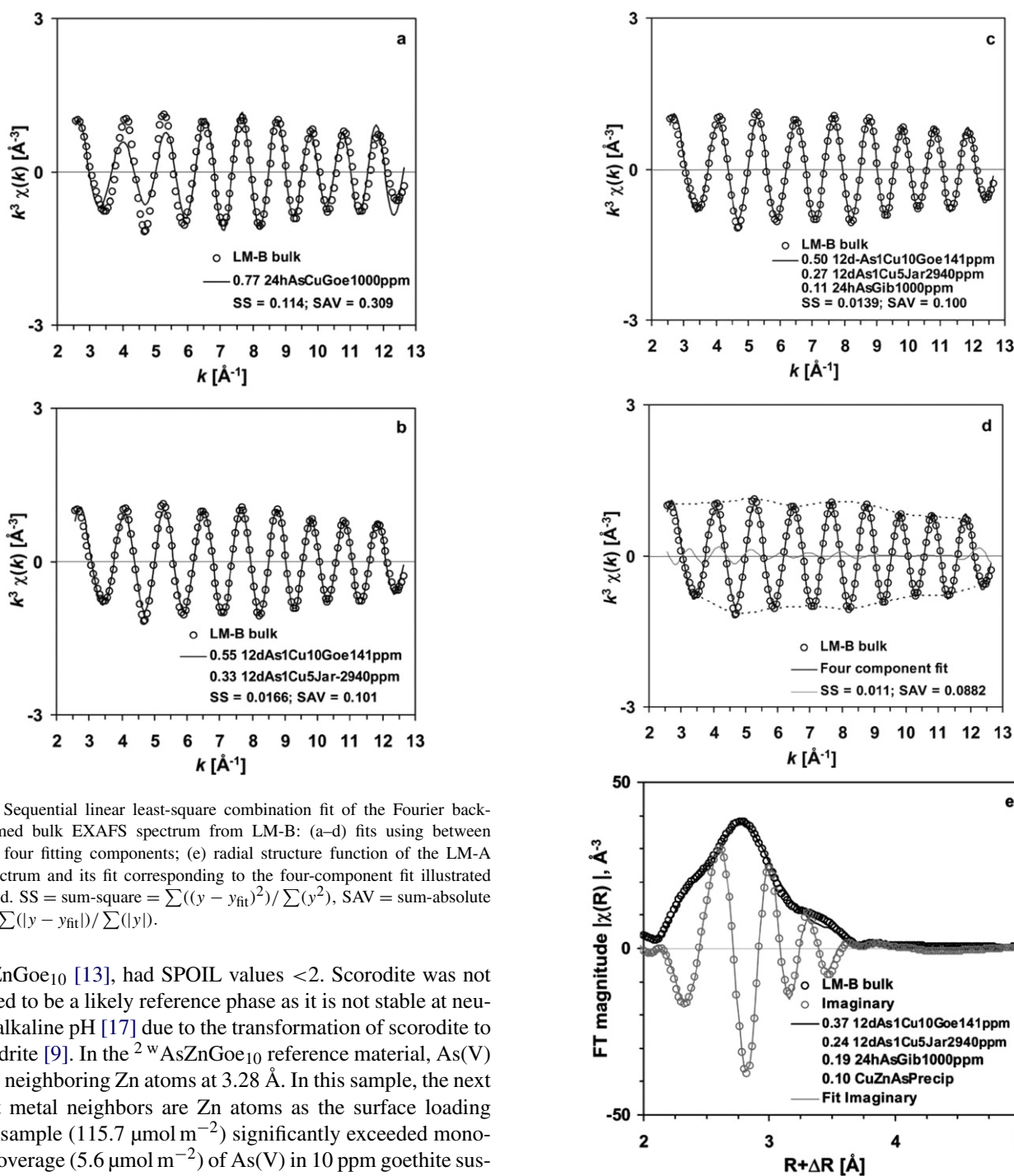
Fig. 11. Sequential linear least-square combination fit of the Fourier back-transformed bulk EXAFS spectrum from LM-B: (a–d) fits using between one and four fitting components; (e) radial structure function of the LM-A bulk spectrum and its fit corresponding to the four-component fit illustrated in Fig. 8d. SS = sum-square = $\sum((y - y_{fit})^2)/\sum(y^2)$, SAV = sum-absolute value = $\sum(|y - y_{fit}|)/\sum(|y|)$.

$^{2\,w}$AsZnGoe$_{10}$ [13], had SPOIL values <2. Scorodite was not expected to be a likely reference phase as it is not stable at neutral to alkaline pH [17] due to the transformation of scorodite to ferrihydrite [9]. In the $^{2\,w}$AsZnGoe$_{10}$ reference material, As(V) has 2.6 neighboring Zn atoms at 3.28 Å. In this sample, the next nearest metal neighbors are Zn atoms as the surface loading of this sample (115.7 µmol m^{-2}) significantly exceeded monolayer coverage (5.6 µmol m^{-2}) of As(V) in 10 ppm goethite suspensions at pH 7 [13]. With increasing SPOIL value, the number of adsorption complexes (ACs) increased from 33 percent (SPOIL < 3.0) to 58 percent (3.0 > SPOIL < 4.5) while the number of intermediate states between adsorption complex and precipitate, or poorly ordered precipitates (POPs) diminished from 17 to 12 percent (SPOIL < 3.0 vs 3.0 < SPOIL < 4.5, respectively). Sixty-six percent (8 out of 12) of the references identified as "good" (SPOIL < 3.0) were either ACs, POPs or precipitated (P/M, M = mineral) phases of As with Cu in which the average As–Cu distance occurred at circa 3.20 and 3.40 Å similar to the two excellent reference phases. References identified as fair (3.0 < SPOIL < 4.5) were dominantly As(V) adsorption complexes on goethite prepared in the presence of

Zn with As–Fe/Zn distances of circa 3.30 ± 0.04 Å suggestive of bidentate binuclear complexes. Interestingly, the As(V) surface complex on jarosite (NaFe$_3$[SO$_4$]$_2$(OH)$_6$), which shows circa 2 Fe atoms at 3.22 Å is also identified as a "fair" reference phase. The similarity of the As–Fe radial distance and CN to many of the copper-arsenate reference phases would suggest that its SPOIL value should be higher, however, its MS$_{As–O–O}$ occurs circa 0.06 Å below that of POPs or ACs of As(V) with Cu (3.03 vs 3.09 Å, respectively) and furthermore does not have contributions from other Fe atoms near 3.40 Å. The absence of
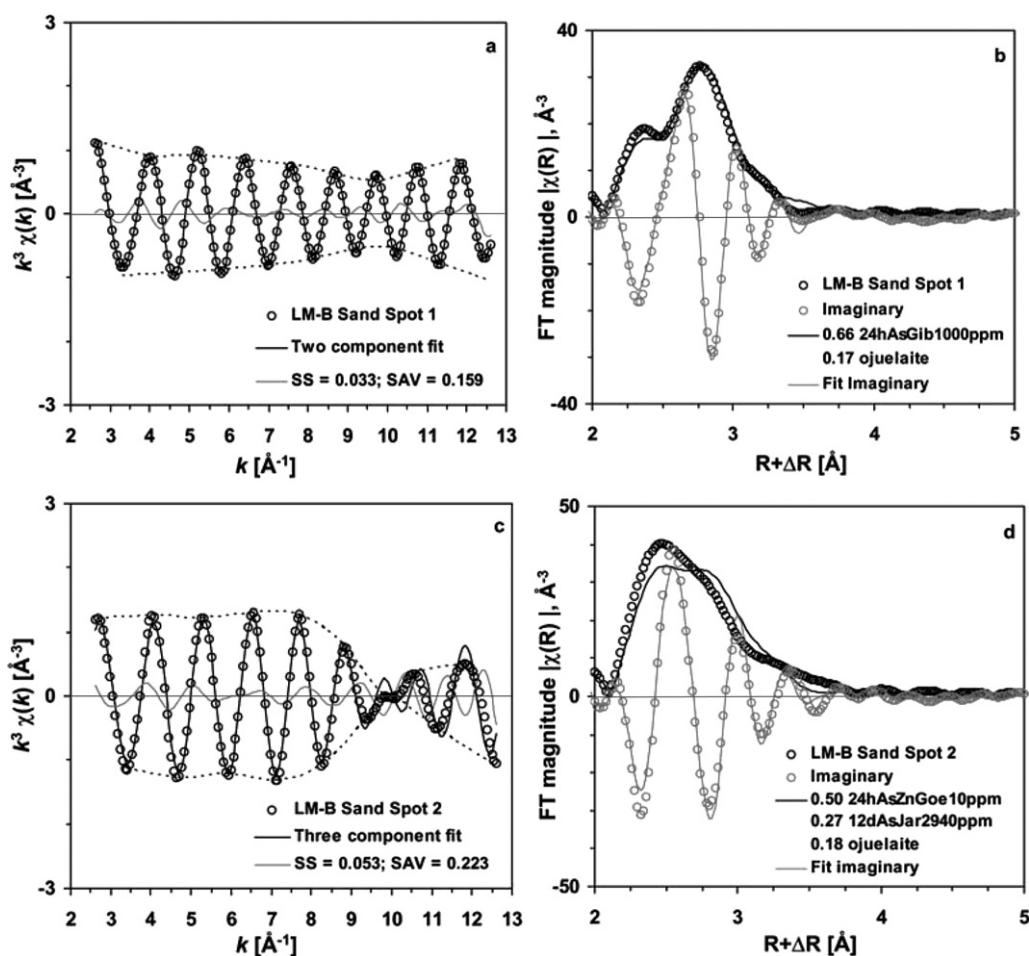
Fig. 12. Linear combination fit of Spots 1 and 2 on LM-B Sand (Fig. 5) showing the fitted k^3-weighted $\chi(k)$ function (a and c) and the corresponding RSFs (b and d). The dashed lines in (a) and (c) outline the absorption envelope of each experimental spectrum. No viable fit could be determined for Spot 3 in Fig. 5.

jarosite peaks in the XRD pattern (Fig. 1a) suggests that this particular reference may represent overall next nearest metallic (Cr, Fe, Cu, or Zn) neighbors at *circa* 3.2 Å rather than As(V) sorbed on jarosite.

3.6. Linear least-square combination fit (LLSF) analysis

Out of 31 spectra, all but 10 spectra could be fit linearly with the available reference phases identified during target analysis. The sum-square (SS) error of the ten unfitted spectra ranged from 0.104 to 0.28 or in four cases could not be ascertained at all. Of the 21 fitted spectra, three reference spectra were required to linearly fit each experimental spectrum with average sum-square values of 0.015 ± 0.009 (LM-A) or 0.034 ± 0.015 (LM-B) (Tables 5 and 6). In five cases, four reference spectra were used to fit the spectra, ensuring that each additional component lowered the SS error by at least 20 percent [27]. In these cases, the fourth component contributed at least eight percent to the experimental spectrum.

The bulk speciation of As(V) in LM-A (0–20 cm) showed that the spectrum was compose 55 percent of the $AsCuZnCr_2O_3$ reference phase, 17 and 8 percent of the $^{12\,d}As_1Cu_5\,Jar_{2940\,ppm}$ and $^{12\,d}As_1Cu_{10}Jar_{2940\,ppm}$ reference phase, respectively, and

12 percent of scorodite (Figs. 8a–8e, Table 5). Each of the four components lowered the sum-square (SS) error by *circa* 56 percent. The two Cu–As(V) co-sorption complexes on jarosite formed at pH 5.5 are indicative of poorly ordered copper-arsenate precipitates, in which As(V) is coordinated by Cu atoms at 3.21, 3.38, and 3.78 Å (Table 3). This bonding environment is most closely related to the average coordination environment of As(V) in clinoclase [38] and is also similar to the coordination environment of As(V) in the mixed copper/zinc-arsenate precipitate ($AsCuZnCr_2O_3$) on eskolaite (α-Cr_2O_3). The presence of scorodite was unexpected but suggests that the soil may have been highly acidic in the past and that scorodite is slowly dissolving (and redistributing) under the current neutral to alkaline pH conditions.

Figs. 9 and 10 show the linear fit results of the three selected spots on Map C (Fig. 3) and of Spots 1 and 2 on Map 2 of the thin section (Fig. 4). Visual inspection of the experimental $\chi(k)$ functions on Map C and TS Map 2 show that phase and amplitude functions are discrepant among the sampled spots, which is well reflected in the differing shapes and modulations of the corresponding FT magnitudes and imaginary phases, respectively, in the RSFs. For example, LM-A Map C Spot 2 has an amplitude function (see dashed outline) that distinctly culmi-

Table 5
Linear least-square combination fit results for μXAFS spectra collected from the LM-A (0–20 cm) depth fraction

LM-A Sample	C1[a]	Amount	C2[a]	Amount	C3[a]	Amount	C4[a]	Amount	Total	SS[b]	SAV[b]
LM-A	$AsCuZnCr_2O_3$	0.55	$^{12d}As_1Cu_5Jar_{2940ppm}$	0.17	Scorodite	0.12	$^{12d}As_1Cu_{10}Jar_{2940ppm}$	0.08	0.92[c]	0.008[c]	0.085[c]
Map C Spot 1	Ojuelaite	0.35	$^{12d}As_1Cu_{10}Jar_{2940ppm}$	0.20	AsCuPrecip	0.14	$^{12d}AsJar_{2940ppm}$	0.10	0.79	0.010	0.09
Map C Spot 2	$^{24h}AsCuZnGoe_{1000ppm}$	0.47	AsCuZnPrecip	0.36	$^{12d}AsJar_{2940pmm}$	0.25		0.00	1.08	0.019	0.141
Map C Spot 3	$^{24h}AsCuGib_{1000ppm}$	0.73	$^{12d}As_1Cu_{10}Jar_{2940ppm}$	0.24	Olivenite	0.09		0.00	1.06	0.009	0.079
Sand Map 1 Spot 1	$^{12d}As_1Cu_{10}Goe_{141ppm}$	0.56	Olivenite	0.35	Adamite	0.09		0.00	1.00	0.024	0.127
TS Map 2 Spot 1	Ojuelaite	0.50	$^{12d}As_1Cu_{10}Jar_{2940ppm}$	0.31	$^{12d}AsJar_{2940pmm}$	0.23	Adamite	0.18	1.22	0.007	0.069
TS Map 2 Spot 2	$^{2w}AsZnGoe_{10ppm}$	0.56	$^{12d}As_1Cu_{10}Jar_{2940ppm}$	0.11	$^{12d}AsJar_{2940pmm}$	0.07		0.00	0.74	0.002	0.04
TS Map 3 Spot 1	$^{24h}AsCuZnGib_{1000ppm}$	0.85	$^{12d}As_1Cu_{10}Jar_{2940ppm}$	0.15		0.00		0.00	1	0.025	0.152
TS Map 3 Spot 2	$^{12d}As_1Cu_{10}Jar_{2940ppm}$	0.38	$^{24h}AsZnGoe_{100ppm}$	0.33	$AsCuZnCr_2O_3$	0.15		0.00	0.86	0.026	0.147
Average		0.55		0.26		0.15		0.12	0.97	0.015	0.106
±	fraction of ...	0.16	fraction of ...	0.09	fraction of ...	0.07		0.04	0.15	0.009	0.039
... OSC	0.00	0.00	0.00	0.00	0.00	0.00	0.00	0.00	0.00		
... AC	0.38	0.21	0.13	0.03	0.43	0.06	0.33	0.04	0.34±0.07		
... POP	0.38	0.21	0.63	0.16	0.00	0.00	0.00	0.00	0.37±0.09		
... P/M	0.25	0.14	0.40	0.10	0.57	0.08	0.33	0.04	0.36±0.04		

[a] C1–4 = components 1–4.
[b] SS = sum-square = $\sum((y - y_{fit})^2)/\sum(y^2)$, SAV = sum-absolute value = $\sum(|y - y_{fit}|)/\sum(|y|)$.
[c] Excluded from fit statistics at the bottom of the table.

Table 6
Linear least-square combination fit results for μXAFS spectra collected from the LM-B (20–40 cm) depth fraction

LM-B Sample	C1[a]	Amount	C2[a]	Amount	C3[a]	Amount	C4[a]	Amount	Total	SS[b]	SAV[b]
LM-B (bulk)	$^{12d}As_1Cu_{10}Goe_{141ppm}$	0.37	$^{12d}As_1Cu_5Jar_{2940ppm}$	0.24	$^{24h}AsGib_{1000ppm}$	0.19	CuZnAsPrecip	0.10	0.90[c]	0.011[c]	0.088[c]
Map A AsHotspot	$^{12d}As_1Cu_{10}Goe_{141ppm}$	0.59	$^{12d}As_1Cu_5Jar_{2940ppm}$	0.16	$AsCuCr_2O_3$	0.19		0.00	0.94	0.019	0.134
Sand Map 3 Spot 1	$^{24h}AsGib_{1000ppm}$	0.66	Ojuelaite	0.17		0.00		0.00	0.83	0.033	0.159
Sand Map 3 Spot 2	$^{24h}AsZnGoe_{10ppm}$	0.50	$^{12d}AsJar_{2940ppm}$	0.27	Ojuelaite	0.18		0.00	0.95	0.053	0.223
SaSiCl Map 2 C-Spot	$^{12d}As_1Cu_{10}Goe_{141ppm}$	0.83	$^{12d}As_1Cu_{10}Jar_{2940ppm}$	0.26		0.00		0.00	1.09	0.063	0.252
SaSiCl Map 2 N-Spot	$^{24h}AsCuGib_{1000ppm}$	0.63	$^{12d}AsJar_{2940ppm}$	0.26	Adamite	0.13		0.00	1.02	0.052	0.191
SaSiCl Map 2 S-Spot	$^{12d}As_1Cu_5Jar_{2940ppm}$	0.65	$AsCuCr_2O_3$	0.23		0.00		0.00	0.88	0.018	0.372
TS Map 1 AsHotspot	$^{24h}AsCuGib_{1000ppm}$	0.68	$^{12d}As_1Cu_5Jar_{2940ppm}$	0.28	$^{6m}AsZnGoe_{100ppm}$	0.10		0.00	1.06	0.022	0.138
TS Map 2 Spot 1	$AsCuCr_2O_3$	0.87		0.00		0.00		0.00	0.87	0.025	0.151
TS Map 2 Spot 2	$AsCuZnCr2O3$	0.36	$^{12d}AsJar_{2940ppm}$	0.26	$^{12d}As_1Cu_5Jar_{2940ppm}$	0.20	$^{24h}As_{2.5}Zn_{2.5}Goe_{1000ppm}$	0.18	1.00	0.036	0.182
TS Map 2 Spot 3	$AsCuCr_2O_3$	0.73	$^{12d}As_1Cu_{10}Goe_{141ppm}$	0.40		0.00		0.00	1.13	0.037	0.185
TS Map 3 Spot 1	$AsCuCr_2O_3$	0.77	$^{12d}As_1Cu_{10}Jar_{2940ppm}$	0.20		0.00		0.00	0.97	0.021	0.144
Average		0.66		0.25		0.16		0.18	0.98	0.034	0.194
±	fraction of ...	0.29	fraction of ...	0.07	fraction of ...	0.04		0.00	0.09	0.015	0.066
... OSC	0.00	0.00	0.00	0.00	0.00	0.00	0.00	0.00	0.00		
... AC	0.36	0.24	0.30	0.07	0.00	0.00	0.00	0.00	0.32±0.10		
...POP	0.18	0.12	0.50	0.12	0.20	0.03	0.00	0.00	0.28±0.05		
... P/M	0.36	0.24	0.20	0.05	0.80	0.13	1.00	0.18	0.60±0.07		

[a] C1–4 = components 1–4.
[b] SS = sum-square = $\sum((y - y_{fit})^2)/\sum(y^2)$, SAV = sum-absolute value = $\sum(|y - y_{fit}|)/\sum(|y|)$.
[c] Excluded from fit statistics at the bottom of the table.

nates near 8 Å^{-1}, whereas Spots 1 and 3 on the same map have lower amplitudes and broader absorption envelopes with a faint beatnode near 6.5 Å^{-1} (Figs. 9a–9f). The reference phases used for fitting the bulk- and μEXAFS spectra in LM-A underline the precipitated nature of As(V) in the upper 20 cm of this soil

as suggested by PCA earlier (*vide supra*). On average 63 percent of all references used to fit spectra collected from LM-A were composed of As and Cu co-sorbed or precipitated phases suggesting that Cu is involved with sequestering As(V). The remaining 37 percent were composed of different As(V) sur-
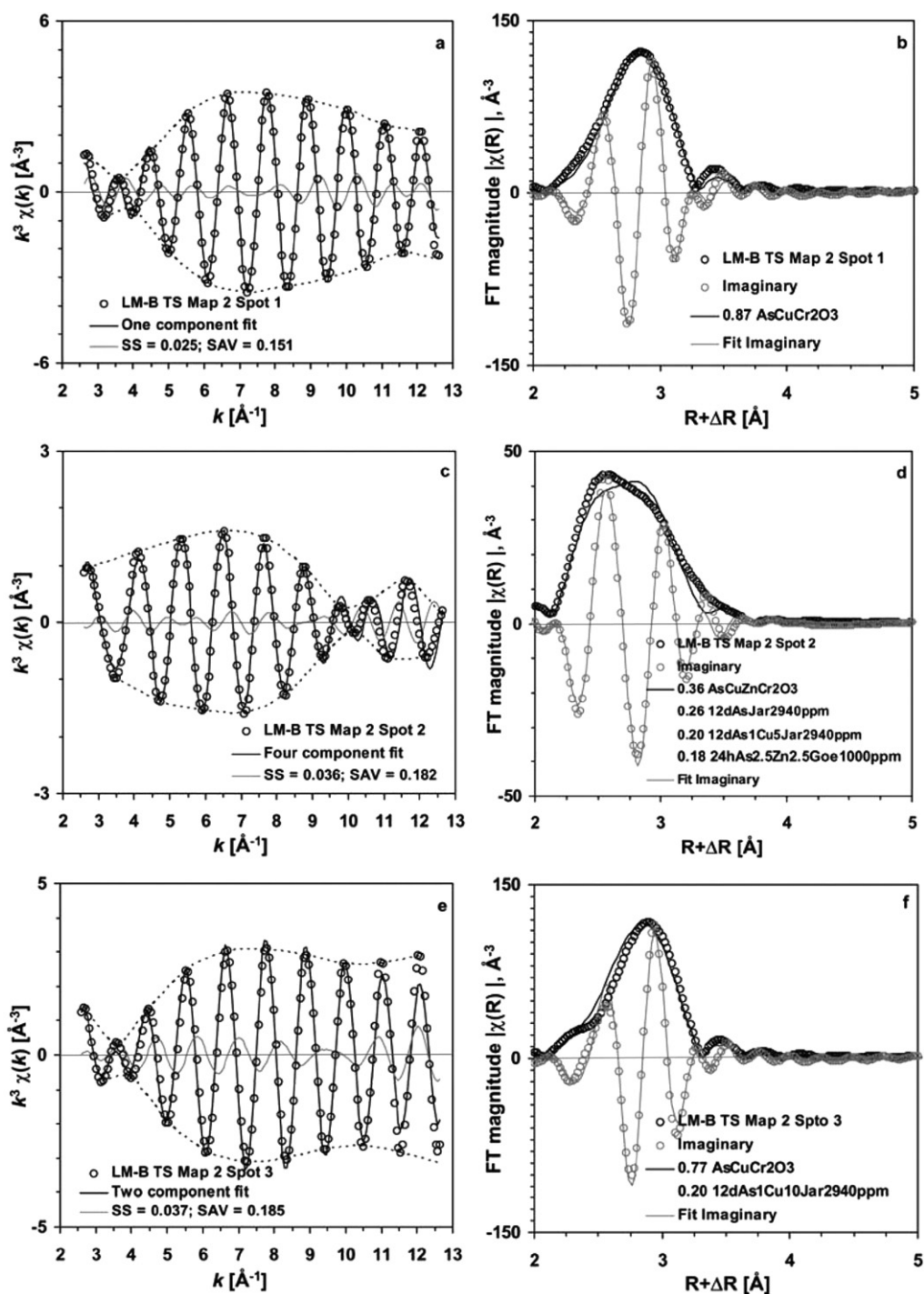
Fig. 13. Linear combination fit of Spots 1–3 on LM-B TS Map 2 (Fig. 6) showing the fitted k^3-weighted $\chi(k)$ function (a, c, and e) and the corresponding RSFs (b, d, and f). The dashed lines in Figs. 10a, 10c, and 10e outline the absorption envelope of each experimental spectrum.

face complexes on goethite in the presence of Zn, As(V) sorbed on jarosite or of mineral phases such as adamite or ojuelaite (Fig. 14a).

Linear fit results of the bulk As spectrum from LM-B (20–40 cm) suggested that it was composed of three similar copper-arsenate phases (0.37 $^{12\,d}$As$_1$Cu$_{10}$Goe$_{pH\,5.5}$, 0.24 $^{12\,d}$As$_1$Cu$_5$Jar$_{pH\,5.5}$, and 0.10 AsCuZnPrecip) comprising 71 percent of the spectrum and 19 percent As(V) adsorption complexes on gibbsite (Figs. 11a–11e, Table 6). In these three

copper-arsenate reference materials, As(V) is coordinated by Cu atoms at the goethite and jarosite surfaces or was homogeneously precipitated (AsCuZnPrecip). Copper atoms near 3.20, 3.30, 3.38, and 3.80 Å are indicative of a clinoclase-like coordination environment for As(V) (Table 3). In contrast to LM-A, it should be noted that the bulk speciation of As(V) in LM-B appears to be less mineralized/precipitated, however, the strong tendency of As(V) to be coordinated by Cu also applied to LM-B. In addition, the main second shell peak of
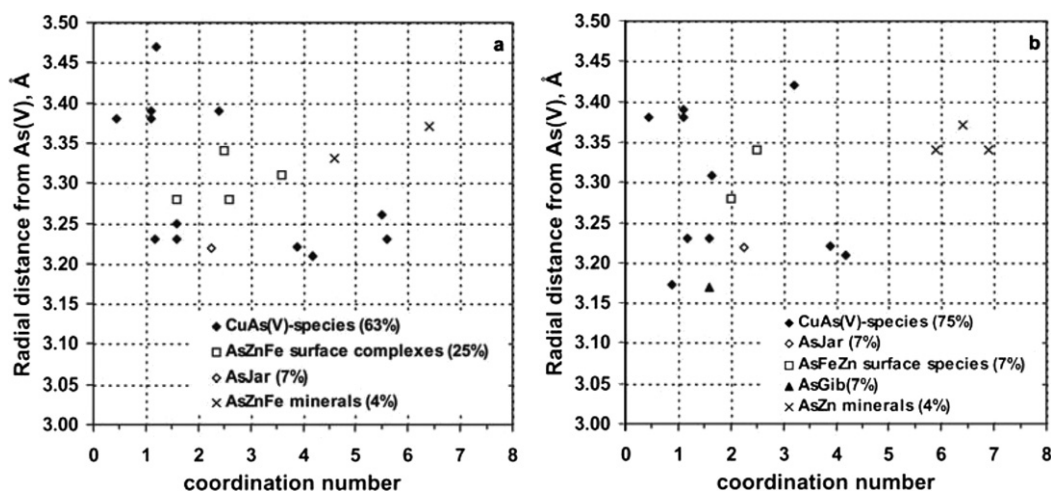
Fig. 14. Scatter plots of coordination number versus radial distance summarizing the linear least-square combination fit analysis for LM-A (a) and LM-B (b). The copper-arsenate species, which are the most abundant phase over the top 40 cm, have a distinct distribution of metal cations near 3.2 and 3.4 Å around As(V). Arsenate adsorbed on jarosite has a similar CN:R coordinate to the copper-arsenate species. Arsenate surface species on iron oxides, have similar coordination numbers, but greater radial distances separating them from the copper-arsenate species. Mineral species of As with Fe or Zn can be distinguished by significantly larger CN.

the LM-B bulk RSF has distinct left- and right-hand shoulder features (Fig. 11e) suggesting contributions from next nearest neighbors at shorter and longer distances than the main contribution near 2.78 Å ($R + \Delta R$, uncorrected for phase shift). The left-hand shoulder feature is fitted by $^{24\,h}$AsGib$_{pH\,7.0}$ contributions ($R_{As-Al} \sim 3.15$ Å), whereas the right-hand shoulder is accounted for by Cu contributions at and above 3.38 Å.

Figs. 12 and 13 show the linear fit results of the selected spots on the "LM-B Sand" map (Fig. 5) and map 2 on the thin section (LM-B TS Map 2, Fig. 6). The depreciation of the goodness of fit for spectra from LM-B is readily apparent from the increased amplitude of the residual $\chi(k)$ functions and the discrepancy among the experimental and fitted Fourier transform magnitudes. The increased error appears to be associated with the lack of a specific As(V) coordination state, possibly with manganese (Mn). In Fig. 5a, As in spot 3 is strongly correlated with Mn (purple colored spot) and a similar correlation to Mn is apparent for Spot 1 in Fig. 6a. The lack of a fit result for Spot 3 in Fig. 5a and the single component fit result (0.87 AsCuCr$_2$O$_3$) of Spot 1 in Fig. 6a suggest that we are missing a distinct coordination environment of As(V), possibly with Mn, but definitively with another constituent that has a short interatomic As-metal distance. This could also be seen from the unfittable RSF of spot 3 in Fig. 5a. Our confidence in the goodness of fit for the fitted spectra remains high though, because the modulations of the experimental and fitted imaginary phases coincided well, suggesting that the FT magnitude discrepancies in the presented RSFs were largely "cosmetic" in nature, i.e., the phase functions are met, but not the amplitude functions. Both phase and amplitude functions vary among the spots selected on map "LM-B Sand" and on map "LM-B TS Map 2" highlighting changes in the average coordination environment of As(V) on hot and soft-spots a few 100 μm apart. Despite the impression of the linear fit result for the bulk EXAFS LM-B spectrum that the average As speciation is less mineralized/precipitated, the number of isolated spots with precipitated As(V) was larger.

On average, 60 percent of all reference spectra used for linear fitting in LM-B were of either mineralized or precipitated As(V) species, with the remaining 40 percent being evenly distributed among ACs and poorly ordered precipitates (POPs). On average 75 percent of all references used to fit spectra in LM-B were composed of either fully precipitated or poorly-ordered copper-arsenate precipitates highlighting the role of Cu in the sequestration of As(V) at this depth (20–40 cm). The remaining 25 percent were respectively composed of As(V) surface complexes on goethite in the presence of Zn, surface adsorption complexes on gibbsite and jarosite or of mineral/precipitated phases such as adamite and adamite-like precipitates (Fig. 14b).

4. Discussion

4.1. Data in perspective

Arsenic occurred mostly as As(V), which is in good agreement with the sandy, well aerated soil profile, the absence of water-logged conditions, and the typical application of As$_2$O$_5$ [39]. The sandy texture of the soil (82 percent sand) and low clay content (3 percent) was indicative of a soil with low specific surface area and consequently a small number of reactive surface sites likely confined to isolated regions where Fe- or Al-hydroxides (e.g., ferrihydrite and gibbsite) coat sand-sized grains or other mineral surfaces. Elevated As fluorescence signals observed in some areas of μSXRF images could be attributed to the precipitation of As with other metals, foremost with Cu, or to regions of high surface site availability from amorphous Fe- and/or Al-oxides where As, Cu, Zn, and Cr accumulated. The principal component and target analyses and linear fit results of the bulk and μEXAFS spectra suggested that both possibilities applied in this soil. In some cases, As occurred as distinct Cu-arsenate precipitates (e.g., LM-B TS Map 2 Spots 1 and 3 and LM-B TS Map 3 Spot 1), whereas in numerous other spots, As(V) appeared to be in association with

Cu(II) as poorly ordered precipitates on gibbsite, jarosite and/or goethite. Indeed, copper-arsenate species comprised more than 60 and 75 percent of reference materials used for linear fitting LM-A and LM-B μEXAFS spectra, respectively (Fig. 14). The remaining 40 and 25 percent could readily distinguished into As surface complexes on goethite in the presence of Zn cations and mineralized As species (e.g., adamite and scorodite). Hereby, it could be noted that in LM-B the mineralized or precipitated species all had adamite-like structure [12,13]. Furthermore, As(V) sorption on gibbsite-like phases was more prominent in LM-B than in LM-A.

The apparent role of Cu in the sequestration of As(V) may be explained by the higher thermodynamic stability of Cu–arsenates (log Ks $= -35.1$, $Cu_3(AsO_4)_2 \cdot 2H_2O$) than for example Zn–arsenates (log Ks $= -27.5$) [40]. At pH 7.0, 10–15 μM of AsO_4 and Cu in solution will form clinoclase-like precipitates, whereas more than 400 μM of Zn and AsO_4 are required to form hydrated koettigite, $Zn_3(AsO_4)_2 \cdot 2.5H_2O$. Mineral surfaces can hereby considerably lower the energy required for precipitate formation. We have recently shown with Zn and arsenate that functional groups on goethite can act as nucleation sites for adamite and koritnigite precipitates, and have observed similar behavior with Cu and arsenate on kaolinite, jarosite, and goethite promoting the precipitation of clinoclase-like phases [18].

Despite the strong indication of Cu sequestering As(V) into copper-hydroxy arsenate complexes, caution should be applied with making overly quick conclusions about which metal cations are indeed responsible for the sequestration of As(V). The local coordination environment of As(V) (and other metal cations) is controlled by the underlying anion layer structure [41]. In the surface adsorbed or two dimensional state, the proximity of next nearest metallic neighbors to As(V) between 3.25 and 3.50 Å are dependent on the specific metal-metal bonding arrangements of the sorbent. For example, in the companion paper of this manuscript, we have highlighted that the average As–Al distance on gibbsite is shorter than the average As–Fe distance on goethite due to the greater interatomic Al–Al distance in gibbsite and the subsequent greater distance between apical Al–O atoms forcing the bidentate-binuclear AsO_4 surface complex closer to the Al metal centers [18]. In the heterogeneous environment of a soil environment, however, there is nothing that precludes the possibility of a similar arrangement to become possible between Al, Fe, Mn, Cu, and Zn atoms. Furthermore, precipitated As(V) species bound as link units into metal-hydroxide structures have longer and shorter As-metal distances which are not necessarily associable with a particular surface adsorption complex, but exist in corner-sharing modes to single metal centers, two, three or four edge-sharing metal centers and or corner-sharing metal cations (e.g., clinoclase). Arsenate adsorbed on jarosite provides a similarly "misleading" coordination environment by coordinating to two Fe atoms with a mean $R_{As–Fe}$ of 3.23 Å (Fig. 14). The absence of jarosite peaks in the XRD pattern suggests that the $^{12\,d}AsJar_{pH\,5.65}$ reference material proxied for As–Cu complexes, however, we can neither be sure that amorphous jarosite is not present, particularly as the presence of scorodite in the

LM-A bulk EXAFS spectrum suggests that this soil may have been strongly acidic (pH < 4) in the past. Consequently, the confidence with which we can point at a specific metal or pair of metals to be responsible for sequestering As(V) is lower than our ability to define the average local coordination environment of As(V) into precipitated, poorly ordered precipitates or surface adsorption complexes based on the magnitude of the coordination number (amplitude function) and the associated radial distance(s) (phase functions) of the next nearest neighbor(s). Distinct metal neighbors could only be ascertained if it was indeed possible to selectively remove individual metal constituents from a heterogeneous material. This is, however, as Fig. 2 and many other sequential extraction studies have shown, practically impossible.

4.2. Environmental aspects

Traditionally there have been three CCA formulations (A, B, and C) in which the elements Cu, Cr(VI), and As(V) were applied as solutions to the wood. The percent content of the mixtures is distributed on average into ca. 20 percent CuO, 35 to 65 percent $Cr^{VI}O_3$, and 16 to 45 percent As_2O_5, thus CCA formulations contain more Cr than As than Cu [5]. This distribution is exactly opposite to the total concentrations of Cu, Cr, and As found in LM-A or LM-B (Fig. 1). Balasoiu et al. [25] showed that for mechanical mixtures of soils ranging from highly mineral soils to highly organic soils, the ratio of total Cu:Cr:As retained in the soil after sequential extraction was similar to the initial application ratio of Cu, Cr, and As. One possibility for explaining the soil's Cu:Cr:As ratio is that the treated wood retained more Cr than As or Cu. Upon application to the wood, Cr(VI) undergoes reduction to Cr(III), which tends to precipitate as $Cr(OH)_3$ s [5]. Independent μXANES investigation of Cr's oxidation state in these soils failed to provide conclusive evidence due to rapid radiation damage (beamline X-26A, NSLS, Brookhaven National Laboratories, Upton NY, USA). An alternative explanation might be that As and Cr (oxyanions) were leached in greater proportion from the soil than copper. Chromate and arsenate adsorption complexes on variably-charged surfaces have lower stability with increasing pH, suggesting that the remediation strategy of increasing pH to stabilize Cu (and Zn) may have lead to increased As and Cr desorption and leaching.

5. Summary and conclusions

Arsenic sorption in metal-contaminated soils does not occur exclusively on the surface sites of clay minerals and Fe- or Al-oxy(hydroxides). Our study has demonstrated that co-contaminating metal cations Cu, Zn, and Cr, but particularly Cu influence the type of As(V) sorption complexes formed in soil. Target analysis and LLSF results suggested a significant (63–75 percent) sequestration of As(V) by Cu(II) with a general tendency of As(V) to occur as precipitated or poorly ordered precipitates, rather than surface adsorption complexes on Fe or Al oxides. Fifty years after the closure of the CCA treatment site where these soils had been collected, the broad spec-

trum of sorption states suggests that As sorption complexes are metastable, and that liming may have promoted the loss of some As and Cr from the upper 40 cm of the soil profile. Future studies of this and other metal-contaminated soils may wish to look at fewer regions of interest over even smaller areas, but expand the spectroscopic investigations to the metal cations suspected of complexing AsO_4. Given the sandy nature of the soil, column leaching tests lend themselves to study the movement of As, Cu, Cr, and Zn through the soil profile. In combination with bulk and micro-focusing techniques, leaching and re-partitioning of As in the lower layers could thus be explored.

Acknowledgments

References

[1] A.H. Welch, D.B. Westjohn, D.R. Helsel, R.B. Wanty, Ground Water 38 (4) (2000) 589–604.

[2] R.S. Oremland, J.F. Stolz, Science 300 (2003) 939–944.

[3] S. Tamaki, W.T. Frankenberger Jr., Rev. Environ. Contam. Toxicol. 124 (1992) 79–110.

[4] E. Smith, R. Naidu, A.M. Alston, Adv. Agr. 64 (1998) 149–195.

[5] J.A. Hingston, C.D. Collins, R.J. Murphy, J.N. Lester, Environ. Pollut. 111 (1) (2001) 53–66.

[6] G.M. Pierzynski, J.T. Sims, G.F. Vance, Soils and Environmental Quality, CRC Press, Boca Raton, FL, 1994.

[7] S. Fendorf, M.J. Eick, P. Grossl, D.L. Sparks, Environ. Sci. Technol. 31 (2) (1997) 315–320.

[8] P.R. Grossl, M. Eick, D.L. Sparks, S. Goldberg, C.C. Ainsworth, Environ. Sci. Technol. 31 (2) (1997) 321–326.

[9] G.A. Waychunas, B.A. Rea, C.C. Fuller, J.A. Davis, Geochim. Cosmochim. Acta 57 (1993) 2251–2269.

[10] S.E. O'Reilly, D.G. Strawn, D.L. Sparks, Soil Sci. Soc. Am. J. 65 (1) (2001) 67–77.

[11] M. Ding, B. de Jong, S.J. Roosendaal, A. Vredenberg, Geochim. Cosmochim. Acta 64 (7) (2000) 1209–1219.

[12] M. Gräfe, M. Nachtegaal, D.L. Sparks, Environ. Sci. Technol. 38 (24) (2004) 6561–6570.

[13] M. Gräfe, D.L. Sparks, Geochim. Cosmochim. Acta 69 (19) (2005) 4573–4595.

[14] R.V. Gaines, H.C.W. Skinner, E.E. Foord, B. Mason, A. Rosenzweig, Dana's New Mineralogy, Wiley, New York, 1997.

[15] D. Paktunc, A.L. Foster, G. LaFlamme, Environ. Sci. Technol. 37 (10) (2003) 2067–2074.

[16] H.W. Langner, C.R. Jackson, R. McDermott, W.P. Inskeep, Environ. Sci. Technol. 35 (16) (2001) 3302–3309.

[17] M. Sadiq, Water Air Soil Pollut. 93 (1997) 117–136.

[18] M. Gräfe, R.V. Tappero, M.A. Marcus, D.L. Sparks, Geochim. Cosmochim. Acta (2007), in press.

[19] M.L. Jackson, Soil Chemical Analysis—Advanced Course, University of Wisconsin, Madison, WI, 1956.

[20] A. Tessier, P.G.C. Campbell, M. Bisson, Anal. Chem. 57 (7) (1979) 844–851.

[21] F. Rapin, A. Tessier, P.G.C. Campbell, R. Carignan, Environ. Sci. Technol. 20 (8) (1986) 836–840.

[22] X.H. Sun, H.E. Doner, Soil Sci. 161 (12) (1996) 865–872.

[23] B. Daus, H. Weiss, R. Wennrich, Talanta 46 (5) (1998) 867–873.

[24] M.J. La Force, C.M. Hansel, S. Fendorf, Environ. Sci. Technol. 34 (18) (2000) 3937–3943.

[25] C.F. Balasoiu, G.J. Zagury, L. Deschenes, Sci. Total Environ. 280 (1–3) (2001) 239–255.

[26] A.C. Scheinost, R. Kretzschmar, S. Pfister, Environ. Sci. Technol. 36 (23) (2002) 5021–5028.

[27] A. Manceau, M.A. Marcus, N. Tamura, in: P. Fenter, N.C. Sturchio (Eds.), Applications of Synchrotron Radiation in Low-Temperature Geochemistry and Environmental Science, Mineralogical Society of America, Washington, DC, 2002, pp. 341–428.

[28] M. Marcus, A.A. McDowell, R. Celestre, A. Manceau, T. Miller, H.A. Padmore, R.E. Sublett, J. Synchr. Rad. 11 (2004) 239–247.

[29] T. Ressler, J. Synchr. Rad. 5 (1998) 118–122.

[30] C. Wang, L.H. Chang, M.S. Yeh, M.C. Lin, F.T. Chung, S.S. Chang, T.T. Yang, M.H. Tsai, Pysica C 441 (1–2) (2006) 277–281.

[31] K.L. Tsang, C.-H. Lee, Y.C. Jean, T.-E. Dann, J.R. Chen, K.L. D'Amico, T. Oversluizen, Rev. Sci. Instrum. 66 (1995) 1812–1814.

[32] S.R. Wasserman, P.G. Allen, D.K. Shuh, J.J. Bucher, N.M. Edelstein, J. Synchr. Rad. 6 (1999) 284–286.

[33] T. Ressler, J. Wong, J. Roos, I. Smith, Environ. Sci. Technol. 34 (2000) 950–958.

[34] E.R. Malinowski, Anal. Chem. 49 (4) (1977) 612–617.

[35] E.R. Malinowski, Anal. Chim. Acta 103 (1978) 359–364.

[36] K.M. Komar, Phytoremediation of arsenic contaminated soils: Plant identification and uptake enhancement, M.S. thesis, University of Florida at Gainesville, 1999.

[37] Y. Arai, E.J. Elzinga, D.L. Sparks, J. Colloid Interface Sci. 235 (1) (2001) 80–88.

[38] R.K. Eby, F.C. Hawthorne, Acta Cryst. C 46 (1990) 2291–2294.

[39] D.C. Bull, P.W. Harland, Wood Sci. Technol. 35 (1–2) (2001) 137–141.

[40] J.P. Gustafsson, Visual Minteq., US-EPA, 2004.

[41] A. Manceau, K.L. Nagy, L. Spadini, K.V. Ragnarsdottir, J. Colloid Interface Sci. 228 (2) (2000) 306–316.

[42] M. Gräfe, D.L. Sparks, in: R. Naidu (Ed.), Managing Arsenic in the Environment: From Soil to Human Health, CSIRO Publishing, Adelaide.